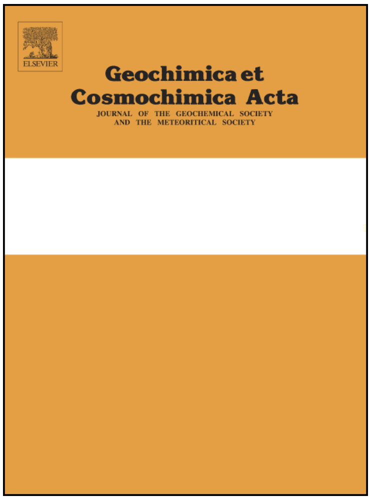

Influence of Al, C, N and H on the iron redox state in the Earth's lower mantle: A geochemical quantum model

Marcello Merli, Costanza Bonadiman, Valentina Brombin, Alessandro Pavese

PII: S0016-7037(25)00046-8
DOI: https://doi.org/10.1016/j.gca.2025.01.035
Reference: GCA 13719

To appear in: *Geochimica et Cosmochimica Acta*

Received Date: 16 January 2024
Accepted Date: 24 January 2025

Please cite this article as: Merli, M., Bonadiman, C., Brombin, V., Pavese, A., Influence of Al, C, N and H on the iron redox state in the Earth's lower mantle: A geochemical quantum model, *Geochimica et Cosmochimica Acta* (2025), doi: https://doi.org/10.1016/j.gca.2025.01.035

Influence of Al, C, N and H on the iron redox state in the Earth's lower mantle: a geochemical quantum model

Marcello Merli[1], Costanza Bonadiman[2,*], Valentina Brombin[2], Alessandro Pavese[3]

[1] *Department of Earth and Marine Sciences, University of Palermo, Via Archirafi 36, 90123 Palermo, Italy*

[2] *Department of Physics and Earth Sciences, University of Ferrara, Via Saragat 1, 44122 Ferrara, Italy*

[3] *Department of Earth Sciences, University of Turin, Via Valperga Caluso 32, 10100 Turin, Italy*

Corresponding author: Costanza Bonadiman

e-mail: bdc@unife.it

Abstract

Iron is the most abundant element by weight in our planet, the dominant component of the core and the only major transition metal in the mantle. Its speciation in the present-day lower mantle remains one of the most controversial aspects to deal with in modelling the deep interiors of the Earth. Here, we present an unconventional approach that relies upon quantum mechanics and the bonding Bader theory to predict the iron oxidation state at lower mantle conditions (24/1900-90/2700 GPa/K) in bridgmanite, the major mineral phase. This approach provides insights into the lower mantle geochemistry on a global scale and a unified viewpoint. The chemical species that on account of their electronic/steric features and mobility expectably induce redox effects on iron in bridgmanite are Al, N, C and H. Hydrogen causes reduction, whereas the other species promote oxidation. The combination of the probability of occurrence of the Al-N-C-H driven reactions with the availability of the involved species points to iron never achieving full oxidation; instead, it reaches a maximum average oxidation number of ~2.4. This is equivalent to a Fe^{3+}/Fe_{tot} ratio that varies with depth from 15.9 to 12.1% (if Al-N-C-H are accounted for), and from 19.3 to 29.0% (if only Al is considered). Iron in the lower mantle is therefore more reduced than previously expected, in terms of ferric fraction, because of the important reducing action of H. If we assume that Fe^{3+} is always associated with iron disproportionation ($3Fe^{2+} \rightarrow 2Fe^{3+} + Fe^{0}$), then the Al-N-C-H atom exchange reactions yield an estimate of metallic iron fraction in the lower mantle as large as ~0.4 wt%. This figure increases up to ~0.8 wt% when neglecting N-C-H effects on ferric iron formation and is fully comparable to the latest experimental result (0.7 wt%) using aluminium only.

Keywords: Fe oxidation number; lower mantle; bridgmanite; REDOX-reactions; Bader theory

1. Introduction

The Fe^{3+}/Fe_{tot} ratio in the Earth's lower mantle affects physical (*i.e.*, radiative heat transfer, mantle temperature profile, subduction slab penetration rate) and chemical (*i.e.,* mantle mineral stability) processes that take place in the deep interiors of our planet and influence the internal structure of the Earth (Frost and McCammon, 2008; Ismailova et al., 2016; Mashino et al., 2020). Despite the crucial role of the Fe^{3+}/Fe_{tot} ratio, the geochemical cycle of ferric iron (Fe^{3+}) is still a matter of debate, mostly pivoting around the key-questions "which reactions are responsible for $Fe^{2+} \rightarrow Fe^{3+}$ and what is the Fe^{3+}/Fe_{tot} fraction in the lower mantle?". Although literature provides a wealth of experimental data on the oxidation state of iron at lower mantle conditions, an overall vision is hampered by the fact that controversial Fe^{3+}/Fe_{tot} figures are reported, and superdeep diamond inclusions do not bear bridgmanite but only retrograde minerals (generally ortho- and clino-enstatite) originated from its decomposition (McCammon et al., 2004; Kamisky et al., 2015; Walter et al., 2022 and reference therein). The back-transformation reactions likely perturbed the Fe oxidation state as a result of decompression and breakdown mechanisms (Kubo et al., 2022; Zedgenizov et al., 2020), so that any direct evidence of lower mantle Fe oxidation state is prevented.

Mashino et al. (2020) claim that their seismic model agrees with bridgmanite (Bdm: IMA–CNMNC, Warr, 2021) bearing a high ferric content that decreases in the middle/deep portion of the lower mantle to Fe^{3+}/Fe_{Bdm}~0.2, so that such a value is compatible with a "Fe^{2+} dominant, silica-enriched Earth's lower mantle model". The most recent ultra-high pressure experiments conducted in laser-heated diamond anvil cells (Zhang et al., 2024) confirm this picture of a lower mantle under hydrous conditions, reporting ferric iron-rich bridgmanite (Fe^{3+}/Fe_{Bdm}~0.6-0.2) at a depth < 2000 km (80-100 GPa) and dominant Fe^{2+} in bridgmanite above 105 GPa.

Conversely, Andrault et al. (2018) and Huang et al. (2021), observe an increase in Fe^{3+}/Fe_{Bdm} with pressure and Al-content, up to ~40-50%. Kurnosov et al. (2017) suggest an Fe^{3+}-rich lower mantle, on account of Fe^{3+}/Fe_{Bdm} ranging from ~0.66 (800 km depth) to ~0.33 (1300 km depth). On a crystal-chemical scale, Kaminsky and Lin (2017), investigating the association of Bdm and Fe-periclase (Fp) in natural juvenile diamond inclusions, conclude that Fp hosts ferrous iron (Fe^{2+}) only, whereas Fe^{3+} occupies the high coordination (12/8) site of the perovskite structure. Otsuka et al. (2013) claim, instead, a potential role of Fp in hosting Fe^{3+}, although in terms of very low concentrations that unlikely can affect the Fe^{3+}/Fe_{tot} balance in comparison with Bdm. Sinmyo et al. (2017), in turn, state that Fe^{2+} prefers the twelve-fold coordination site of the perovskite structure, whereas Fe^{3+} can be hosted by both cuboctahedral/dodecahedral and octahedral sites. As to the electronic configuration of ferrous and ferric iron in a perovskite structure at high pressure and temperature, Kupenko et al. (2015) point out that Fe^{3+} preserves a high-spin (HS) configuration and predominantly occupies high coordination sites, whereas Fe^{2+} takes an intermediate spin state (IS).

Several authors claim iron disproportionation (*i.e*., $3Fe^{2+} \rightarrow 2Fe^{3+} + Fe^0$) as the main mechanism to account for Fe^{3+} in Al-bearing systems, because of the occurrence of metallic iron among the observed products of the Bdm forming reactions (Mao and Bell, 1977; Frost et al., 2004). Dorfman et al. (2021) underline the absence of Fe-disproportionation in their Al-free experiments, which give Fe^{2+}-Bdm and Fp (33-128 GPa and 1900-3000 K range). All this suggests that aluminium is a key species in controlling Fe redox reactions.

It is worth recalling the *HP-HT* experimental and theoretical studies that led to the discovery of iron oxides with unconventional oxidation states, such as FeO_2 (Hu et al., 2019) and Fe_5O_6 (Lavina and

Meng, 2016), thus pointing to unusual chemical valence and bonding interactions that hint at a new picture of the redox equilibria inside the Earth.

The present work aims to be a contribution to the debate by:

- introducing an unconventional calculation scheme, which relies upon the bonding Bader theory (Bader, 1990; 2007) and the forward-backward reactions formalism, to model the oxidation number of iron as a function of pressure and temperature, along a geotherm. We assume all of the crystal sites of bridgmanite are occupied either by cations or by anions, so that the Fe's redox state is controlled by atomic replacements involving cations with an oxidation number smaller than silicon's, anions with an absolute oxidation number larger than oxygen's and excess species that potentially affect the electronic basin of iron. Consequently, we shall see that the redox state of iron is the result of a complex balance involving the electronic basins of all of the atoms involved, rather than an electronic exchange restricted to oxygen;
- estimating the Fe^{3+}/Fe_{Bdm} and Fe^{3+}/Fe_{Bdm+Fp} fractions to frame the lower mantle oxidation state related to iron on a global scale.

Quantum mechanics is employed to develop calculations, assuming that Bdm is the sole mineral among the major lower mantle phases that can accommodate ferric iron along with the species involved in Fe-oxidizing reactions, even at the lowest plausible level of oxygen fugacity (Frost and Myhill, 2016). The pressure range 24-90 GPa is chosen to definitely exclude the occurrence of majorite/ringwoodite and post-perovskite phases in the uppermost and lowermost portions of the lower mantle, respectively (Murakami et al., 2004; Frost and Myhill, 2016).

2. Materials and Methods

2.1 Oxidation state modelling

Changes of the conventional oxidation state (or oxidation number) of various chemical species are observed to occur at extreme *P-T* conditions (Qian et al., 2016; Wang et al., 2020), as also predicted by *ab-initio* evolutionary techniques (Oganov and Glass, 2006). The process of moving electrons from one atom to another in a substance is more complex than what the conventional notion of oxidation number describes. In fact, in 2016 the International Union of Pure and Applied Chemistry (IUPAC) recognized that "oxidation state" must be associated with the atomic "*electronic basin*" that allows calculation of the related electronic charge (Karen et al., 2016). This implies a link between the oxidation state of an atom and its electron density $\rho(\boldsymbol{r})$. The key-point is to determine a region around an atom, "*atomic basin*", where the electrons lying within are ascribable to that atom. The electronic charges of individual atoms in crystals can be calculated on the basis of the Bader Theory (Bader 1990; 2007) that exploits the properties of $\rho(\boldsymbol{r})$. Atoms are separated from each other by surfaces (Ω-surface), called "*zero flux surfaces*" , which fulfil the following constraint:

$$\int_0^{\Omega} \nabla\rho(\boldsymbol{r}) \cdot \boldsymbol{n}(\boldsymbol{r}) dS = 0$$

where: $\boldsymbol{n}(\boldsymbol{r})$=versor normal to the Ω –surface at $\boldsymbol{r}$; dS=infinitesimal surface element.

The volume confined by a Ω-surface defines the region of space whose electronic charge does not vary with time, that is

$$\int_0^{\Omega} \rho(r) dV = N_{\Omega}$$

Therefore, N_{Ω} is the *net charge* attributable to the basin of a given atom, and allows calculation of its actual oxidation state. It is worth stressing that using such an approach, the oxidation state is expressed by a real number, which depends on P-T and is not necessarily an integer.

In the present work, the focus is on how charge-coupled cation/anion replacements affect the iron basin charge with respect to the reference Bdm, whose formula unit is $Mg_{1-x}Fe_xSiO_3$ (x=0.1), in which we assume Fe to occur as Fe^{2+}.

We shall use the term "*redox reaction*" to address any reaction that modifies the Fe basin, changing iron's net charge and thereby its oxidation number. It then follows that Fe oxidation/reduction is seen as a process, which reflects a complex readjustment through charge transfers between the atomic basins of *all* the species forming the system. We adopt the difference between iron basin charges of wüstite (FeO) and hematite (Fe_2O_3) as a reference for full iron oxidation, $Fe^{2+} \rightarrow Fe^{3+}$. Both wüstite and hematite are modelled using their *ideal* compositions, which allows them to be used as reference Bader basins related to Fe^{2+}, in the case of the former, and to Fe^{3+}, in the case of the latter. In doing so, we neglect the occurrence of defects in the *real* wüstite $Fe_{(1-x)}O$ (Hidayat et al., 2015; Zakeri et al., 2023).

2.2. Assumptions and driving reactions

2.2.1 Fundamental reactions

The bridgmanite reference composition $(Mg_{0.9}Fe_{0.1})SiO_3$ [Bdm.ref] is calculated on the basis of estimates of the bridgmanite/Fe-periclase Fe^{2+} partitioning coefficients (Sakai et al., 2009; Sinmyo and Hirose, 2013; Merli et al., 2017), in keeping with both homogenous and layered reference bulk mantle models (Javoy et al., 2010; Kurnosov et al., 2017; McDonough et al., 2016).

This leads to the following general question: which *atomic exchange reactions* (also referred to as *atomic replacement reactions*) lead Bdm.ref to a new bridgmanite [Bdm(Mg,Fe,A)] wherein part of Fe^{2+} is turned into Fe^{3+}?

This is formalized through the general exchange reaction:

$$\text{A} + \text{Bdm.ref}(\text{Mg},\text{Fe}^{2+},\text{B}) = \text{Bdm}(\text{Mg},\text{Fe}^{3+},\text{Fe}^{2+},\text{A}) + \text{B} \qquad (1.a)$$

where "A" (chemical species not present in Bdm.ref and incorporated by Bdm) replaces "B" (chemical species present in Bdm.ref, i.e., Mg-Si-O). The A and B species are exchanged with an ideal (virtual) thermodynamic particles reservoir (hereafter "reservoir"), *via* a forward/backward reaction (as in equ.1.a) turning Bdm.ref into Bdm, and *vice-versa*, which continues until the system reaches dynamic equilibrium (Denbigh, 1981; Merli et al., 2020). Dynamic equilibrium is achieved at the Gibbs energy minimum, implying the invariance of the composition and abundance of the system's components. The fundamentals of the particle reservoir are summarized in Supplementary Material A.

To better visualize mass and charge balance of chemical reactions involving atomic substitutions, we use the Kröger-Vink notation (Kröger, 1972) to write the conventional charge-coupled cation/anion replacement equation. A species can be incorporated in a crystal either as an interstitial or as a substitutional defect at one site, both of which naturally require fulfilment of electron-neutrality. The superscripts $^{\bullet}$ and $'$ indicate one positive and one negative charge, respectively, in a crystal. Subscripts refer to the chemical species replaced in a given site. Using the Kröger-Vink notation equ. (1.a) is then rewritten as:

$$\mathrm{A}(reservoir)\overset{\text{Bdm.ref}}{\Longleftrightarrow}\mathrm{A}'_{\mathrm{B}}+\mathrm{Fe}^{\bullet}_{\mathrm{Fe}}. \qquad (1.b)$$

Therefore, “A” can be incorporated into the Bdm.ref lattice as substitutional defect of species B. Charge compensation is obtained with $Fe^{2+} \rightarrow Fe^{3+}$, in the Fe site.

Possible charge-coupled cation/anion exchange equations of the type (1.b) can be categorized into two main classes:

cation substitution: $\mathrm{Z}(reservoir)\overset{\text{Bdm.ref}}{\Longleftrightarrow}\mathrm{Z}'_{\mathrm{Si}}+\mathrm{Fe}^{\bullet}_{\mathrm{Fe}}$ (2.a)

anion substitution: $\mathrm{X}(reservoir)\overset{\text{Bdm.ref}}{\Longleftrightarrow}\mathrm{X}'_{\mathrm{O}}+\mathrm{Fe}^{\bullet}_{\mathrm{Fe}}$ (2.b)

where Z and X have conventional oxidation state $^{3+}$ and $^{3-}$ respectively.

2.2.2 Choice of the “Z” and “X” chemical species

Given that experiments (Irifune et al., 2010; Andrault et al., 2018) and calculations (Zhang and Oganov, 2006) point to a central role for aluminium in the iron oxidation processes, we focus on the charge-coupled cation substitution of equ.(2.a) with Z=Al, in keeping with Al being a major lithophile element of the silicate Earth. Preliminary calculations carried out on the cation site exchange $^{[6]}Fe + ^{[12]}Al \Leftrightarrow ^{[6]}Al + ^{[12]}Fe$ yielded that the probability of the left-hand side configuration is < 1/3 of the probability of the occurrence of the right-hand side member; therefore, Al and Fe are assumed in six-fold and twelve-fold coordination respectively (Mohn and Trønnes, 2016; Huang et al., 2021). Please, note that the site occupied by Mg in the perovskite-type structure is characterised by two classes of cation-oxygen lengths: one has eight bond lengths < 2.2 Å, whereas the other has four bond lengths > 2.4 Å (Fu et al., 2014). This leads to a coordination either eight-fold (dodecahedral) or twelve-fold (cuboctahedral), as a function of a tilting of the octahedron, which is facilitated by undersized cations (Fei et al., 2020);. The perovskite-type structure here used for Bdm exhibits a twelve-fold coordination site. We also neglect *vacancy assisted* charge-coupled cation exchange, such that $Fe^{2+} + Mg^{2+} + Mg^{2+}$ is replaced by $Fe^{3+} + Fe^{3+} + \square$, given that: i) vacancies are supposed to mainly affect anions, *i.e.*, oxygen, without immediate implications upon $Fe^{2+} \rightarrow Fe^{3+}$ (Mohn and Trønnes, 2016; Grüninger et al., 2019 Fei et al., 2020); ii) preliminary calculations indicate that this is the unlikeliest mechanism among those investigated in the case of a composition like the Bdm.ref’s.

Among the charge-coupled anion substitutions, we identify as the best “candidates” for “X” in equ.(2.b) C and N, owing to their electronic (possible reduction state higher than O: $N^{3-} \rightarrow N^{3+}$; $C^{4-} \rightarrow C^{4+}$) and steric (atomic number comparable to O) properties (Hazen et al., 2013; Yoshioka et al., 2018), and their relevance in the geochemical cycle of the Earth’s mantle.

Despite the intrinsic high capacity of N and C to modify their electronic basins, their solubility in bridgmanite is comparatively low (N= 1-23ppm; Yoshioka et al., 2018; Fukuyama et al., 2023) or very low (C = < 1 ppm; Shcheka et al., 2006). This implies that most of the nitrogen and carbon is expected to be stored in other phases, such as carbide and nitride (Armstrong et al.; 2015; Li et al., 2017), or carbonate (Davis et al., 2024). For completeness, we include in the present calculations, the contributions of C and N, whose probability to be incorporated is duly accounted for.

In our modelling we allowed the Bdm's structure to relax at the explored pressure values and observed that C and N invariably changed their initial position tending towards the site left vacant by oxygen. In the case of C, we also tested its capacity to replace Si, obtaining results, in terms of defect-like formation energy, *i.e.*, $E[\mathrm{Bdm(Mg,Fe^{3+/2+},C)}]-E[\mathrm{Bdm.ref(Mg,Fe^{2+})}]+E(\mathrm{O})-E(\mathrm{C})$, that definitely make such a configuration highly unlikely. This is in keeping with the observations of Shcheka et al. (2006), who do report a substitution of Si with C, but at an extent not above the detection limits of the employed analytical techniques.

Eventually, we add to equ.(2.a) and (2.b) a third reaction, characterised by the occurrence of an excess of hydrogen as a free, potentially oxidizing species. The high mobility of H (Hu and Mao, 2021), even under extreme *P*-*T* conditions, and its multi-varied reactivity (*i.e.,* H_2, instead of OH, in H*P* $CaTiO_3$-pervoskite, and H-Fe in a metal alloy in combination with effects related to the Grotthuss mechanism) make the redox behaviour of hydrogen not straightforwardly predictable (Hou et al., 2021; Hu and Mao, 2021; Tsuchiya and Thompson, 2022; He et al., 2023).

Whereupon we introduce:

$$\mathrm{H}(reservoir) \xLeftrightarrow{\mathrm{Bdm.ref}} \mathrm{H}_i' + \mathrm{Fe}_{\mathrm{Fe}}^{\bullet} \qquad (2.c)$$

supposing H to be an interstitial free hydrogen atom in bridgmanite and H^- its anion resulting from a charge transfer from iron. This hypothesis must be tested, and the effects induced by hydrogen will be determined by calculations and accounted for accordingly.

The redox reactions (2.a-c) are modelled by quantum-mechanics methods to reconstruct the Bdm's electron density and determine the Fe basin, from which the oxidation number is calculated *via* the Bader theory (Merli and Pavese, 2018). We use the following atomic replacement reactions, written in the notation of their net chemical equations with respect to bridgmanite according to (1.a):

$$(\mathrm{Mg_{1-x}Fe^{2+}_x})\mathrm{SiO_3} + x\,\mathrm{H}_{reservoir} = (\mathrm{Mg_{1-x}Fe^{2+,3+}_x})\mathrm{SiO_3} \cdot x\,\mathrm{H} \qquad (3.a)$$

$$(\mathrm{Mg_{1-x}Fe^{2+}_x})\mathrm{SiO_3} + x\,\mathrm{N}_{reservoir} = (\mathrm{Mg_{1-x}Fe^{2+,3+}_x})\mathrm{Si(O_{3-x}N_x)} + x\,\mathrm{O}_{reservoir} \qquad (3.b)$$

$$(\mathrm{Mg_{1-x}Fe^{2+}_x})\mathrm{SiO_3} + x\,\mathrm{Al}_{reservoir} = (\mathrm{Mg_{1-x}Fe^{2+,3+}_x})\mathrm{(Si_{1-x}Al_x)O_3} + x\,\mathrm{Si}_{reservoir} \qquad (3.c)$$

$$(\mathrm{Mg_{1-x}Fe^{2+}_x})\mathrm{SiO_3} + x\,\mathrm{C}_{reservoir} = (\mathrm{Mg_{1-x}Fe^{2+,3+}_x})\mathrm{Si(O_{3-x}C_x)} + x\,\mathrm{O}_{reservoir} \qquad (3.d)$$

where x=0.1. Equ.(3.a-d) indicate exchanges of atomic species between two Bdm compositions and a virtual particle reservoir until the conditions of dynamic chemical equilibrium are achieved (please, see Supplementary Material B). In this context we estimate the "*probability of occurrence*" ($\wp$) that corresponds to the chance of a substitution of type (3.a-d) to take place in Bdm; $\wp$, in turn, quantifies the *intrinsic tendency* of Bdm to host the jth-substitution and depends on *x*-*P*-*T* only.

In the next part, we shall use unconventional statements like, for instance, "Al oxidizes Fe", "Al acts as an oxidizing agent" or "Al oxidizing capacity", meaning that the cation replacement reaction (3.c) yields an iron with a basin giving an oxidation number larger than 2+, *i.e.*, the one we assume in the reference bridgmanite. However, an analysis of all the atomic basins (Bader model) shows that oxygen actually reduces, whereas Si, Al, Mg and Fe undergo oxidation, though according to charge transfers that lead to oxidation numbers even diverting from their conventional values.

2.3. Iron's oxidation state determination

The quantities related to the electronic reservoir of iron are addressed using the notation

$$\int_0^{(Fe),\mathrm{j}} \rho(r)dV = Q_{Fe,\mathrm{j}} \tag{4.a}$$

where $Q_{Fe,\mathrm{j}}$ is the *Fe basin charge* induced by the j^th^-reaction of (3.a-d). The related "*Bader oxidation state*" of Fe *(*$oxFe_{\mathrm{j}}$*)* is then provided by:

$$oxFe_{\mathrm{j}} = 2 + \frac{\Delta Q_{Fe,\mathrm{j}}}{\Delta Q_{Fe-ref}} \tag{4.b}$$

where:

1) $\Delta Q_{Fe,\mathrm{j}} = Q_{Fe,\mathrm{j}} - Q_{Fe,\mathrm{Bdm.ref}}$; $Q_{Fe,\mathrm{Bdm.ref}}$= basin charge of Fe^{2+} in reference Bdm, that is $(Mg_{0.9}Fe_{0.1})SiO_3$;

2) $\Delta Q_{Fe-ref} = Q_{Fe2+,\mathrm{wü.ref}} - Q_{Fe3+,\mathrm{hem.ref}}$; $Q_{Fe2+,\mathrm{wü.ref}}$ = basin charge of Fe^{2+} in reference wüstite, that is FeO; $Q_{Fe3+,\mathrm{hem.ref}}$ = basin charge of Fe^{3+} in reference hematite, that is Fe_2O_3; ΔQ_{Fe-ref}= reference difference between basin charges ascribed to Fe^{2+} and Fe^{3+}.

The "*average* (<>) *Fe basin charge*" associated with a given reaction (equ. 3.a-d) is introduced as follows:

$$< Q_{Fe,\mathrm{j}} >= \wp(\mathrm{j}) \times Q_{Fe,\mathrm{j}} + (1 - \wp(\mathrm{j})) \times Q_{Fe,Bdm.ref} \tag{5.a}$$

where $\wp$(j) indicates the abovementioned probability of occurrence of the j^th^-reaction and depends on pressure and temperature (see equ. A.4), where P and T are related to one another through the geothermal model of the layered mantle of Katsura et al. (2010) and Merli et al. (2016). The "*average Fe oxidation state*" induced by the j^th^-reaction (3.a-d), $<oxFe_{\mathrm{j}}>$, is provided by:

$$< oxFe_{\mathrm{j}} >= 2 + \frac{\Delta < Q_{Fe,\mathrm{j}} >}{\Delta Q_{Fe-ref}}, \tag{5.b}$$

where $\Delta{<}Q_{\mathrm{Fe,j}}{>}={<}Q_{\mathrm{Fe,j}}{>}-Q_{Fe,\mathrm{Bdm.ref}}$.

Eventually, we define the "*total average Fe oxidation state*" in Bdm by summing up the $<oxFe_{\mathrm{j}}>$s determined by equ.(5.b):

$$< oxFe >= \sum_{\mathrm{j}=1}^{4} \Pi_{\mathrm{j}} \times < oxFe_{\mathrm{j}} > \tag{6}$$

where "Π_{j}" is the available abundance of the j^th^-oxidizing species (j=H, Al, C, N), entering Bdm.

The fractions associated with the conventional oxidation states of Fe, *i.e.*, ferric ($x_{\mathrm{Fe3+}}$) and ferrous ($x_{\mathrm{Fe2+}}$) iron, are calculated from either the total average oxidation state (*i.e.*, $<oxFe>$) or the average oxidation state of each reaction (*i.e.*, $<oxFe_{\mathrm{j}}>$):

$$(< oxFe >, < oxFe_{\mathrm{j}} >) = 2 \times x_{\mathrm{Fe2+}} + 3 \times x_{\mathrm{Fe3+}} \tag{7}$$

where $x_{\mathrm{Fe2+}}=1- x_{\mathrm{Fe3+}}$. It is worth noticing that in equ.(6) the effects due to Al, N, C and H add up linearly. In this view, correlations between the redox agents are neglected, though they are likely to play a role in natural processes. Therefore, equ.(6) represents a "first order approximation" of the general problem of how redox reactions affect the Fe oxidation state. Calculations were carried out as described in Supplementary Material C, using lower mantle elementary abundances and the electron basis set reported in Supplementary Material D (Table D.1 and Table D.2, respectively).

2.4. Iron speciation estimate

We assume that iron in the lower mantle occurs as Fe^0, $Fe^{2+}{}_{Fp}$, $Fe^{2+}{}_{Bdm}$ and $Fe^{3+}{}_{Bdm}$, which represents an approximation that accounts for most of the observations in terms of experiments and findings, though it neglects $Fe^{3+}{}_{Fp}$. Merli et al. (2017) provide the average composition of Fp, $(Mg_{1-x}Fe_x)O$ $x=0.175-0.379$ (see Fig.6 by the quoted authors in the above mentioned paper), and the partitioning constant $Kd=[x(Fe)/x(Mg)]_{LM-Fp}/[x(Fe)/x(Mg)]_{Fp}$ as a function of P-T, so that $Kd=0.64-0.00824\times P(GPa)$ (LM-Fp represents the Fe and Mg bearing mineral assemblage of the lower mantle, not including Fe-periclase). Equating LM-Fp to an ideal bridgmanite, it is possible to estimate Fe_{Bdm}/Fe_{Fp}, under the condition that iron occurs as ferrous, only. Such an approximation has little effect on the estimate of Fe_{Bdm}/Fe_{Fp}, if the $\mathrm{Fe}_{\mathrm{Bdm}}^{3+}/\mathrm{Fe}_{\mathrm{Bdm}}^{2+}$ ratio that will be determined and discussed below is taken into account. In fact, the average x_{Fe} in the bridgmanite formula unit of Merli et al.(2017) would change from 0.12, total Fe^{2+}, to 0.107, if the following partitioning $0.75Fe^{2+}+0.25Fe^{3+}$ is used (see the ensuing sections for the Fe^{3+}/Fe_{Bdm} calculation).

As to Fe^0, conceptually, charge-coupled cation replacements of equ.(1.a-b) are consistent with a class of complex reactions occurring simultaneously and that can be either Fe-disproportioning or *not* Fe-disproportioning. A case of Fe-disproportioning reaction is:

$$3(Mg_{1-x}Fe_x)SiO_3+(Mg_{1-x}Al_x)(Si_{1-x}Al_x)O_3+3xMgO=2(Mg_{1-x}Fe_x)(Si_{1-x}Al_x)O_3+(2+x)MgSiO_3+xFe \tag{8.a}$$

whereas two examples of non Fe-disproportioning transformations are provided by:

$$2(Mg_{1-x}Fe_x)SiO_3+(Mg_{1-x}Al_x)(Si_{1-x}Al_x)O_3+2xMgO+1/2xO_2=2(Mg_{1-x}Fe_x)(Si_{1-x}Al_x)O_3+(1+x)MgSiO_3 \tag{8.b}$$

and:

$$2(Mg_{1-x}Fe_x)SiO_3+(Mg_{1-x}Al_x)(Si_{1-x}Al_x)O_3+3/2xMgO=2(Mg_{1-x}Fe_x)(Si_{1-x}Al_x)O_3+(1+1/2x)MgSiO_3+1/2xSi \tag{8.c}$$

Equ.(8.a) and (8.c) suggest the potential co-existence of a Fe-Si alloy with ferric iron bearing Bdm in the lower mantle. Concurrently, on the basis of equ.(8.b) a contribution to the Fe^{3+}content in Bdm is still envisaged through the charge-coupled exchange involving $Si^{4+}+Fe^{2+}$and $Al^{3+}+Fe^{3+}$, leaving iron disproportionation aside and supposing instead a reaction driven by $f(O_2)$, as also suggested by previous experimental/thermodynamic modelling (Huang et al., 2021).

All this depicts a complex geochemical scenario, in which the ferric iron content in the lower mantle is modelled following a general description by juxtaposing different potential chemical reactions to be weighted with each other. Yet, a prevalence of the reactions' type (8.a) is supposed, because iron metal is commonly recorded as a reaction product in experiments (Mergner et al., 2021) and observed in natural findings (Li et al., 2012; Bindi et al., 2020), in keeping with previous calculations (Zhang and Oganov, 2006). Therefore, assume that Fe^{3+} is *always* associated with iron disproportionation, $3Fe^{2+}\rightarrow 2Fe^{3+}+Fe^0$, implying $Fe^{3+}/Fe^0=2$.

We can now lay down the set of equations that follow

$$\mathrm{Fe}_{\mathrm{tot}} = \mathrm{Fe}^0 + \left(\mathrm{Fe}_{\mathrm{Fp}}^{2+} + \mathrm{Fe}_{\mathrm{Bdm}}^{2+}\right) + \mathrm{Fe}_{\mathrm{Bdm}}^{3+} = \mathrm{Fe}^0 + \mathrm{Fe}^{2+} + \mathrm{Fe}^{3+} \tag{9.a}$$

$$\varepsilon = \frac{\mathrm{Fe}^{3+}}{\mathrm{Fe}^{2+} + \mathrm{Fe}^{3+}} \tag{9.b}$$

$$\mathrm{Fe}^{3+} = 2 \times \mathrm{Fe}^{0} \tag{9.c}$$

where Fe^0, $\mathrm{Fe}^{2+} = \mathrm{Fe}^{2+}_{\mathrm{Fp}} + \mathrm{Fe}^{2+}_{\mathrm{Bdm}}$, $\mathrm{Fe}^{3+} = \mathrm{Fe}^{3+}_{\mathrm{Bdm}}$ and $\mathrm{Fe}_{\mathrm{tot}}$ are the fractions of metal iron, ferrous iron and ferric (in bridgmanite only) iron, total iron in the lower mantle; ε is calculated using the $\mathrm{Fe}_{\mathrm{Bdm}}/\mathrm{Fe}_{\mathrm{Fp}}$ ratio estimated as stated above, and the $\mathrm{Fe}^{3+}_{\mathrm{Bdm}}/\mathrm{Fe}^{2+}_{\mathrm{Bdm}}$ ratio here predicted. Therefore, we have three variables and three constraints, those provided by equ.(9.a-c), which makes this system univocally solvable, setting $\mathrm{Fe}_{\mathrm{tot}}$ equal either to a normalized or to an estimated value.

3. Results

We recall here that Al-C-N-H will be *unconventionally* addressed as "redox agents", meaning that such species yield iron's basin change with respect to Fe in reference Bdm.

The Bader model (Bader, 1990; 2007) allows us to determine the intrinsic behaviour of iron in Bdm, independently of the natural abundancies of the redox species under investigation.

Figure 1 reports the Bader Fe-oxidation state calculated by equ.(4.b), $oxFe_j$, where j= H, N, Al, C. In general, aluminium, nitrogen and carbon lead to an iron oxidation state that shifts towards Fe^{3+} 's with P. As expected, this is related to an increase in the charge transfer between atoms, favoured by a decrease in the interatomic distances. Carbon is the weakest oxidant and does not induce the complete charge transfer $\mathrm{Fe}^{2+} \rightarrow \mathrm{Fe}^{3+}$ in the explored P-T interval (Fig. 1.a), yielding an iron oxidation number between ~2.6 (24 GPa) and ~2.8 (90 GPa). Nitrogen, also, does not allow a full charge transfer, and iron achieves its highest oxidation number ($oxFe_{\mathrm{N}}$=2.95) at 90 GPa. Only aluminium makes Fe reach its full oxidation at ~40 GPa (Fig. 1.a), thus showing that the replacement of Si with Al is the most effective mechanism, among those investigated, in terms of potential oxidizing capacity. Although room condition-electronegativity values (χ) point to hydrogen as a possible candidate in promoting the oxidation of iron (χ(H)-χ(Fe)≈0.3), H, by contrast, causes a remarkable increase in the electron population of the iron basin with respect to Fe^{2+}, regardless of pressure ($oxFe_{\mathrm{H}}$: 0.87 - 0.92, from 24 to 90 GPa; Fig. 1b). Therefore, hydrogen comparatively promotes Fe-reduction. A concern in modelling H is that its high mobility and thermal motion are neglected in the context of static calculations. For this reason, we tested a variety of random starting positions for hydrogen, sited about 1.5 Å Fe apart. We invariably observed that under structure relaxation the H-atom tended to approach oxygen atoms and stabilize at a O-H distance of about 1 Å. This, on the one hand, suggests a propensity to hydroxyl-like group formation, and on the other hand, provides an explanation about the reducing mechanism that H exerts on Fe. Should hydrogen abandon an oxygen atom under the effect of thermal motion, we expect that it will jump to another site still providing a hydroxyl-like bond, remaining in the cuboctahedral cage of Bdm that hosts Fe and thus leaving the iron electron basin unaffected.

The intrinsic redox capacity of C, N, Al, and H expressed through the Bader oxidation state is tuned by the probability of occurrence, $0 \leq \wp(reaction) \leq 1$, of the reactions (3.a-d) that model the incorporation of these species into Bdm, regardless of the natural abundances of the redox species.

The aluminium oxidizing reaction has the highest probability of occurrence, [$\wp$(Al) >0.41], with a slight tendency to reduce its effects at higher pressure (Fig. 2): $\Delta\wp$(Al) ≈ –6.7% [$\Delta\wp$=($\wp(\mathrm{Al})_{90\mathrm{GPa}}$-$\wp(\mathrm{Al})_{20\mathrm{GPa}}$)/<$\wp(\mathrm{Al})_{20\text{-}90\mathrm{GPa}}$>].

Hydrogen triggers the second most probable reaction between 24 and 40 GPa [$\wp$(H): from 0.36 to 0.34], characterised by a rapid decrease in $\wp$(H) with increasing P ($\Delta\wp$(H) ≈ –68%). The N-driven reaction, in turn, shows: i) a probability of occurrence comparable to H's in the shallow portion of the lower mantle [$\wp$(N): ~0.33; $P < 30$ GPa]; ii) a modest increase, on average, in $\wp$(N) with P up to 80 GPa [$\Delta\wp$(N) ~ 7.6%]; iii) a remarkable increase in $\wp$(N) at 90 GPa, where it reaches the figure of Al. The carbon reaction probability of occurrence remains low [$\wp$(C): 0.08-0.15] throughout the explored P-T interval (Fig. 2).

The average Fe oxidation state, $<oxFe_j>$, calculated by equ.(5.b), links the Bader Fe oxidation state to the probability of having the related exchange j^th^-reaction. $<oxFe_j>$ does not exceed 2.44 (Fig. 3), meaning that none of the species under study is able to fully oxidize iron from ferrous to ferric. Aluminium and nitrogen, as expected, provide the most efficient oxidizing action, whereas C modestly affects the ferrous state of Fe. Conversely, H induces a strong reducing effect, leading iron towards an unconventional Fe^{1+} (Fig. 3). Note that $<oxFe_j> \leq oxFe_j$ (*i.e.*, "Bader Fe oxidation number") because of the depressing effect due to the probability of occurrence of the oxidizing reactions, save the case of $<oxFe_H>$, in which $\wp$(H) decreases with P-T, thus making the occurrence of the H-triggered reduction reaction progressively more unlikely (Figs. 2 and 3).

The average oxidation numbers of iron in Bdm as a function of P-T (Fig. 3) are recast into the conventional way to represent Fe in stoichiometric reactions (*i.e.*, $Fe^{2+}$and Fe^{3+}). The fractions of ferric iron (x_{Fe3+}) in Bdm (Fig. 4), ascribable to each of the reactions under investigation, are obtained by equ.(7). As expected, the trends of x_{Fe3+} mimic those of Figure 3, and the resulting negative Fe^{3+} fraction due to H (not reported in Fig. 4) reflects its reducing action on iron. Over the P range 24-90 GPa we estimate that C causes oxidation,< leading iron to a maximum of 11% Fe^{3+} at 80 GPa (Fig. 4). The nitrogen oxidizing reaction yields a Bdm with 28-33% Fe^{3+} over the P range 24-80 GPa, achieving the highest ferric iron content of 39% at 90 GPa. Bridgmanite originated from the Si/Al substitution reaction bears 41-44% Fe^{3+}.

4. Discussion

The actual iron oxidation number, as determined by the intrinsic contributions of the redox species, provides a source of information to model the reducing-oxidizing behaviour at the global scale of the lower mantle. First of all, we have to take the chemical species' abundances in the lower mantle into account.

4.1 Earth's lower mantle abundances of iron and redox species

Abundance estimates of the Earth mantle's chemical species potentially partitioned in Bdm and involved in the reactions (3.a-d) are summarized in Table D.1 of Supplementary Material D . The Fe content in the lower mantle is well constrained through the Earth's density estimates and amounts to as much as ~6.2-7.0 wt% (Zhang and Oganov et al., 2006; Irifune et al., 2010; Javoy et al., 2010; McDonough, 2016). This range is shared by homogeneous and layered geochemical models (Javoy et al., 2010; McDonough, 2016) of the Earth's mantle. We chose to use the value of 6.26 wt% Fe, coherently with Bdm and Ca-perovskite phase proportions of 81 and 6%, respectively; the remainder is provided by Fp (Javoy et al., 2010; Frost and Myhill, 2016; McDonough, 2016; Merli et al., 2017).

The aluminium abundance, which agrees with homogeneous and layered primitive mantle geochemical models, lies in the range ~1.11-2.38 wt%; we used for our calculations a bulk Al-content as large as 2.01 wt% (Table D.1 of Supplementary Material D), taking the mentioned proportions of Bdm and Ca-perovskite into account.

Present mantle nitrogen estimates, which are provided by measurements Yoshioka et al., 2018, Fukuyama et al., 2023) and thermodynamic calculations (Marty, 2012; Johnson and Goldblatt, 2015; Hirschmann, 2018) , exhibit variable values and are affected by large uncertainties, because of a high sensitivity to the employed model. This approach provides as large a nitrogen content as possible (~ 1 ppm) neglecting its primary fractionation between the forming atmosphere and the Earth's interior (Hirschmann, 2018; Kurokawa et al., 2022; Fukuyama et al., 2023).

The H_2O storage capacity of the lower mantle is still under debate, since studies do not converge on its solubility in Bdm. As summarized by Ohtani, (2022) and Lu and Li (2023), experimental results show a H_2O content in Bdm spanning over three orders of magnitude. The solubility of H_2O in Bdm is potentially influenced by a combination of variables including chemical composition, pressure, temperature, and oxygen fugacity (Merli et al., 2016; Muir & Brodholt, 2018; Yang et al., 2023). Taking all these factors into account, the maximum H_2O storage in the lower mantle may be estimated ~1000 ppm (H ~ 112 ppm), if the total H budget in the Earth's lower mantle is determined only on the basis of the extant figures of the H_2O content in Bdm (Fu et al., 2019; Yang et al., 2023; Purevjav 2024).

Yet, owing to the possible incorporation of H in nominally anhydrous minerals, the H total budget calculated only on the basis of the solubility of hydroxyl in minerals may be underestimated. Therefore, we chose the bulk H_2O estimates determined from cosmochemical constraints and numerical calculation on accretion (~680-3800 ppm; Ohtani, 2021). On the basis of the mean value of ~2000 ppm H_2O, we calculated that a maximum of 225 ppm of H is potentially available for the redox reaction as in equ. (3.a).

In comparison with nitrogen and hydrogen, carbon exhibits a different behaviour, because of i) its lower solubility in the main mantle minerals (Shcheka et al., 2006) and ii) its metal/silicate partitioning coefficient that is much higher than the ones of N and H (Hirschmann, 2016; Dalou et al., 2017). Given that the lower mantle is supposed to host a total of ~1 wt% of metals (Frost et al., 2004; Huang et al., 2021), the available carbon partitioning coefficients lead to an average amount of C ranging from 100 to 450 ppm (Marty, 2012; Hirschmann, 2018); in the light of this, we use the value of 400 ppm, around which most estimates cluster (Sun and Dasgupta, 2023). Although carbon solubility in Bdm (~ 0.1-0.5 ppm) is at least one order of magnitude lower than those of N and H (Shcheka et al., 2006), the intrinsic effects of C in modifying the electronic basin of iron are taken into account (equ 3.d).

Both $Fe_{Bdm}/(Al+N+C+H)$ mole and $Fe_{Bdm}/(Al)$ mole are < 1. This guarantees that the set of chosen oxidizing species is always sufficient to provide their saturation of the Fe redox reactions in Bdm.

4.2 Iron speciation I: ferric iron fraction in bridgmanite

Aluminium is expected to be the most effective oxidizing species, among those explored, as suggested by the Bader oxidation state (Fig. 1) and the probability of occurrence of the oxidizing Al-reaction (Fig. 2). Fe^{3+} fractions in bridgmanite (x_{Fe3+}) ascribable to Al do not remarkably change with pressure; only above 70 GPa the efficacy of Al is slightly reduced (Fig.4). This tendency is counterbalanced by the aluminium solubility in bridgmanite that instead significantly increases with increasing pressure (Merli et al., 2020; Liu et al., 2016). The aluminium contents in bridgmanite, estimated by the degree of substitution Si/Al and Mg/Al, at fixed Fe = 0.1 a.p.f.u (eq 3.c), in equilibrium reactions of a closed system (Merli et al., 2020), vary with pressure from 0.17 a.p.f.u (24 GPa) to 0.25 a.p.f.u

(90 GPa). These values agree with previous results obtained by theoretical modelling and experiments on Mg-Al bridgmanites (Merli et al., 2020; references therein).

In contrast with aluminium, hydrogen exhibits a negative correlation with Fe^{3+}, as displayed by Figs.(1) and (3), promoting a partial reduction of iron. This agrees with the recent findings of Zhang et al. (2024), who observe a negative slope of the Fe^{3+}/Fe_{Bdm} ratio in a hydrous sample with composition $(Mg_{0.85}Fe_{0.15})SiO_3$, thus concluding that H_2O helps the stabilisation of ferrous iron in Bdm, at least in the lower mantle regions approaching the core-mantle boundary.

The collective contribution from H, Al, N and C to the formation of the Fe oxidation number in Bdm is determined by taking their relative abundances in the lower mantle into account (see equ.(6) and Table D.1 of Supplementary Material D. Aluminium and hydrogen account for about 82.5 and 16.7% of the Fe oxidation number on average, respectively, in the explored *P*-*T* range, whereas N and C provide a very modest total contribution (0.68 %). It is worth noticing that H induces a reduction effect partly counterbalancing the oxidation due to the other species. Should we take the maximum H_2O content compatible with solubility in bridgmanite (1000 ppm; Fu et al., 2019; Yang et al., 2023; Purevjav 2024), the contribution of hydrogen to the Fe-oxidation number would decrease to 9.13%.

The fraction of ferric iron in Bdm, resulting from the summation of the positive (Al, N, C) and negative (H) contributions, ranges from 22.5 to 26.3%, and follows a weakly positive trend with *P* (Fig. 5). Our estimates are compared with the extant experimental data so far obtained using Bdm compositions similar to those of this study. In general, a comparison between theoretical results and measurements is difficult because of the scattering of the latter, which depends on a complexity of aspects, such as experimental setup, starting materials used for syntheses, and resulting Bdm compositions. Yet, the tendency of Fe^{3+}/Fe_{Bdm} to slightly increase with pressure is qualitatively shared by our results and the experimental observations of Huang et al. (2021), who predicts a flattening of the increasing trend at $P > 40$ GPa; our calculations yield figures ranging below those of Huang et al. (2021) (Fe^{3+}/Fe_{Bdm} ~38-42%; Fig.5a). If we set the H abundance of the lower mantle as large as the maximum H_2O-content soluble in Bdm, the fraction of ferric iron in bridgmanite increases in the explored *P*-range from ~22-26 to ~31-32%, nearing the experimental data of Huang et al. (2021).

Instead, Andrault et al. (2018) report on average Fe^{3+}/Fe_{Bdm} values closer to those in this paper, but with a steeper positive trend with *P* (from ~13% at 24 GPa to ~35% at 90 GPa). The mentioned authors relate this slope and the comparatively "small" Fe^{3+}/Fe_{Bdm} ratio at low pressure to the occurrence of Al-bearing phases that host aluminium in competition with Bdm; at higher pressure Bdm is the sole phase accommodating Al (up to 0.17 a.f.u).

The Fe^{3+}/Fe_{Bdm} intervals from earlier determinations (Sinmyo et al., 2011; Prescher et al., 2014; Kupenko et al., 2015; Piet et al., 2016; Shim et al., 2017) are displayed in the inset of Figure (5), but no single comparison is performed on our results, because of the irregularity of the *P* -*T* range explored and the high variability of the resulting Bdm compositions, in terms of Al and Fe contents.

If we restrict ferric iron formation to the Al-driven reaction only, thus mimicking anhydrous conditions, the Fe^{3+}/Fe_{Bdm} ratio drastically increases (42.8% on average); the Fe^{3+}/Fe_{Bdm} *versus P* profile peaks at 44.5% at ~50 GPa, and beyond it changes into a downward-sloping, convex curve that flattens at ~80 GPa (Fig. 5). Therefore, values and profiles from modelling reveal the role of H in affecting the ferric iron content in Bdm. In fact, taking an Al-only bearing model into account, our predictions of Fe^{3+}/Fe_{Bdm} agree with the results of Huang et al. (2021) and approach those of Andrault et al. (2018) at $P > 70$ GPa (Fig. 5). All this is in keeping with the fact that, as far as we know, H, C and N were not added to the starting materials in the Bdm syntheses for Fe^{3+}/Fe_{Bdm} determination; therefore, the resulting ferric iron depends only on the Al contents introduced into the system.

4.3. Iron speciation II: implications for the lower mantle

Solving equ.(9.a-c), we are able to determine the speciation of iron in the lower mantle. Calculations have been performed taking the H estimates by cosmochemical /numerical modelling (Marty et al., 2012; Ohtani, 2024) that account for the potential contributions other than that related to the H solubility degree in Bdm (H_2 and superionic phases; Yang et al., 2016; Hu and Mao, 2021). In fact, solubility is taken into account by the occurrence probability of each reaction.

Considering Bdm as a part of the Earth's lower mantle Fe-bearing assemblage (Bdm+Fp), the total ferric fraction, *i.e.*, $Fe^{3+}/Fe_{(Bdm+Fp)}$, changes trend with respect to the Fe^{3+}/Fe_{Bdm}'s. The resulting $Fe^{3+}/Fe_{(Bdm+Fp)}$ values range between 15.3% (24 GPa) and 12.2% (90 GPa), with a gentle deflection downwards at ~60 GPa (Al-N-C-H profile; Fig. 6). This behaviour is mainly justified by the partitioning of iron and hydrogen between Bdm and Fp: (Mg,Fe)O tends to progressively modify its composition by incorporating more and more Fe and H with pressure (Prescher et al., 2014; Merli et al., 2016; 2017). A significant change occurs, if Al only is taken into account: the $Fe^{3+}/Fe_{(Bdm+Fp)}$ values lie within the interval 29.9-19.3%, with a sharp decrease in ferric iron that starts at ~40 GPa (Fig.6; Al-only). The difference between the cases of Al-N-C-H and Al-only is related to accounting for or *not* accounting for hydrogen, which combines with and counterbalances aluminium as a function of P. Note that both curves definitively flatten at $P \geq 80$ GPa (Fig. 6).

Our modelling based on the general exchange reactions given by equ.(3.a-d) led us to estimate ferric and ferrous contents without explicitly resorting to disproportionation that, in turn, is ubiquitously invoked in association with the charge-coupled cation substitution $Fe^{2+}+Si^{4+} \rightarrow Fe^{3+}+Al^{3+}$ (1.b) in Bdm, by previous experimental investigations (Frost et al., 2004; Kurnosov et al., 2017; Andrault et al., 2018).

If bulk lower mantle Fe amounts to ~6.3 wt% (Table D.1 of Supplementary Material D) and the inferred Fe^{3+}/Fe_{tot} ratio ($Fe_{tot}=Fe^{2+}+Fe^{3+}+Fe^0$) weakly depend on P, then the Fe^{3+} estimate yields an average figure as large as ~0.8 wt% (Fig. 6; Al-N-C-H involved). This, in turn, leads, *via* a disproportionation reaction, to a flat Fe^0 curve, with an average of ~0.4 wt%, corresponding to ~6-7% of Fe_{tot} in the lower mantle. Such a figure is lower than the latest estimate of 0.7 wt% (~12% Fe_{tot}), experimentally obtained using lower mantle bulk iron and Al-in-Bdm contents similar to ours (Huang et al., 2021). This comparatively small Fe^0 content from modelling agrees with the *quasi*-overlapping (in the range of the degree of confidence) of the Fe^{3+}/Fe_{tot} and $Fe^{3+}/Fe_{(Bdm+Fp)}$ curves displayed in Figure 6, when Al-N-C-H are involved. To balance the experimental 0.7 wt% Fe^0 by the sole disproportion mechanism, the quoted authors calculate that Fe^{3+}/Fe_{Bdm} and Fe^{3+}/Fe_{tot} ratios of 0.50 and 0.28, respectively, are required in the lower mantle region 24-50 GPa (Fig. 6). Our modelling predicts Fe^{3+}/Fe_{tot} and Fe^0/Fe_{tot} values in agreement with those of Huang et al., (2021), in the same P range, if we neglect the effects of H in determining Fe^{3+}/Fe_{Bdm}, and by consequence Fe^{3+}/Fe_{Bdm+Fp} (Fig. 6).

It is established that a large fraction of Earth's hydrogen, the most abundant element in the solar system, is still stored in the lower mantle (Marty, 2012), supposedly as hydroxyl (OH) in hydrous and nominally anhydrous minerals (Merli et al., 2016; Ohtani, 2021), and in the Core Mantle Boundary region, probably associated with iron alloys (Piet et al., 2023). Therefore, it is unlikely that hydrogen does not take part in the redox mechanisms occurring in the Earth's interior; nevertheless, experiments have not been designed so far, to our knowledge, to explore the simultaneous effects of Al and H.

One of the relevant results of the present paper is the potential important role of H as a reducing agent, capable of mitigating the Fe-oxidation induced by the aluminium-silicon substitution, leading from an average $Fe^{3+}/(Fe_{Bdm}+Fe_{Fp})$ ratio of 23.8 (Al only) to14.1% (including Al-N-C-H). In such a view, we expect, on a global scale, that the higher the content of the H-excess, the less Fe^{2+} undergoes oxidation to Fe^{3+}, and the lower mantle is Fe^{0}-poorer. Altogether, we foresee Fe^{3+} and Fe^{0} contents in the lower mantle to range between two extremes: the maximum ferric iron contents, in which Al is the only effective oxidizing agent and the minimum ferric iron contents, in which H is called into play. Nitrogen and carbon contributions are small, but not negligible, to the lower mantle oxidation state on a global scale.

A very general chemical frame accounting for both disproportioning and not disproportioning reactions pivots around the system $Fe\text{-}Si\text{-}O_2$, summarized by equ.(8.a-c). The $Fe\text{-}Si\text{-}O_2$ system describes how lithophile mantle's major elements can stabilize metal phases in the various portions of the Earth's mantle at highly reduced conditions (Foley, 2011; Mao et al., 2017). The FeSi-phase can form in a "pure" silicate system at very low oxygen fugacity [logfO_2(IW~-2): Andrault et al., 2018; Huang et al., 2021] and remains solid with B2-structure at the *P-T* conditions of the lowermost portion of the Earth's mantle (Lord et al., 2010). High *P-T* nuclear inelastic scattering experiments on FeSi phase revealed sound velocity values significantly lower than those of other mineral phases under the same conditions, coherent with the occurrence of high-density/ultralow-velocity zones (ULVZs) at the Earth's core-mantle boundary (CMB) (Fischer et al., 2013). Hence, FeSi is expected to settle at the CMB as a component of the discontinuous ULVZs. This view is in keeping with the hypothesis that considers FeSi as a product of the silicate Earth, rather than a core/mantle chemical reaction.

5. **Conclusions**

In this study we investigated the speciation of iron in bridgmanite (Bdm), providing insights into the redox state of the lower mantle on a global scale, employing a unified viewpoint. The oxidation number of iron as a function of pressure and temperature, was determined by an unconventional approach that relies upon quantum mechanics and the bonding Bader theory. Charge-coupled cation ($Al\rightarrow Si$)/anion($N,C\rightarrow O$) replacements and excess H-content affect the iron basin charge inducing redox reactions that change the oxidation state of Fe with respect to ferrous iron assumed in a reference Bdm of composition $Mg_{1-x}Fe_xSiO_3$ (x=0.1). On the basis of our results (pure Bader Fe-oxidation state), carbon is the weakest oxidant and does not induce the complete charge transfer $Fe^{2+}\rightarrow Fe^{3+}$ in the explored *P-T* interval, yielding an iron oxidation number between ~2.6 (24 GPa) and ~2.8 (90 GPa). Only aluminium makes Fe reach its full oxidation at ~40 GPa, thus pointing to the replacement of Si with Al as the most effective mechanism, among those investigated, in terms of oxidizing capacity. Hydrogen, conversely, causes an increase in the electron population of the iron basin with respect to Fe^{2+}, regardless of pressure ($ox\mathrm{Fe}_H$: 0.87 - 0.92, from 24 to 90 GPa), promoting Fe-reduction thereby. The average oxidation state of iron induced by each of the involved chemical species is modelled by combining the Bader Fe-oxidation state and the probability of occurrence ($\wp$) of every exchange reaction. This yields flat trends for all of the species investigated, and a maximum average oxidation state for iron of 2.44, due to aluminium and corresponding to the largest Fe^{3+} fraction of ~44%. If the redox reactions associated with Al, C, N and H are weighted as a function of the element abundance in the lower mantle and considered all together, then the calculated Fe^{3+}/Fe_{Bdm} ratio is affected foremost by aluminium

and hydrogen, ranging from ~22 to ~42% and in agreement with the experimental results obtained using lower mantle bulk iron and Al-in-Bdm contents comparable to ours. Considering Bdm as a part of the Fe-bearing lower mantle assemblage (bridgminite +Fe-periclase), the ferric fraction, i.e., $Fe^{3+}/Fe_{(Bdm+Fp)}$, ranges between 15.3% (24 GPa) and 12.2% (90 GPa). If we couple disproportionation (ubiquitously invoked in association with the charge-coupled cation substitution $Fe^{2+}+Si^{4+}\rightarrow$

Fe^{3+}+Al^{3+} in Bdm) with our forecast of $Fe^{3+}/(Fe^{2+}+Fe^{3+})$ and assuming ferric iron to enter Bdm only, then we obtain Fe^{3+}/Fe_{tot} and Fe^{0}/Fe_{tot} values in agreement with those measured (Huang et al., 2021) in the same *P* range , neglecting the effects of H. Experiments have not been designed so far, to our knowledge, for exploring the effects due to the combination of Al and H, therefore divergent values are expected between experiments and modelling. However, it is unlikely that hydrogen does not take part in the redox mechanisms occurring in Earth's interior. In general, the larger the content of the H-excess, the less Fe^{2+} undergoes oxidation to Fe^{3+}, and the poorer of Fe^{0} is the lower mantle. Although nitrogen and carbon can replace oxygen, their contributions to Fe^{3+} are small, but not negligible, on account of a very low abundance estimated in the lower mantle.

In this light, we foresee Fe^{3+}/Fe_{tot} and Fe^{0}/Fe_{tot} ratios in the lower mantle to lie in the ranges (20-29%) and (9-13%), when Al is the only effective oxidizing agent, and (13-15%) and (6-7%) if H-C-N are called into play. Fe^{0}/Fe_{tot} estimates accounts for a possible presence of FeSi phase as a component of the discontinuous ULVZs. This view is in keeping with the hypothesis that considers FeSi as a product of the silicate Earth, rather than a core/mantle chemical reaction.

CRediT authorship contribution statement

Marcello Merli: Formal analysis, Validation, Conceptualization, Software. **Costanza Bonadiman:** Conceptualization, Investigation, Methodology, Data curation, Writing- Original draft preparation. Writing- Reviewing and Editing. **Valentina Brombin:** Data curation, Writing- Reviewing and Editing, Visualization. **Alessandro Pavese:** Conceptualization, Investigation, Methodology, Formal analysis, Data curation, Writing- Reviewing and Editing, Supervision.

Acknowledgements

The present study was granted by the "PRIN2017-2017L83S77" project of the Italian Ministry for Education, University and Research (MIUR) (AP; CB). V.B was supported by University of Ferrara Research Fund 2021 (FAR.L-BC_037; CB). The Authors are thankful to two anonymous Reviewers and the Associate Editor for corrections and suggestions, which actually improved the quality of the manuscript.

Data availability

All data generated or analysed during this study are included in this published article (and its appendices and supplementary information files)

Appendix A. Supplementary material

In the Supplementary Material, we provide: (**A**) "Reservoir", about the thermodynamic fundamentals of this model; (**B**) "Reaction model", about the solutions of equ.(3.a-d); (**C**) "Calculations", about the computing strategy that has been chosen; (**D**) .Table D.1: Estimates of the contents in the lower mantle of iron and the other redox species (Al, C, N, H) explored in this study; Table D.2: Basis sets used in the present investigation.

References

Armstrong, L.S., Hirschmann, M.M., Stanley B.D. et al. 2015. Speciation and solubility of reduced C–O–H–N volatiles in mafic melt: implications for volcanism, atmospheric evolution, and deep volatile cycles in the terrestrial planets. Geochim Cosmochim Acta 171:283–302.

Andrault, D., Muñoz, M., Pesce, G., Cerantola, V., Chumakov, A., Kantor, I., Pascarelli, S., Rüffer, R., Hennet, L., 2018. Large oxygen excess in the primitive mantle could be the source of the Great Oxygenation Event. Geochem. Persp. Let. 6, 5–10.

Bader, R. F., 1990. Atoms in Molecules: A Quantum Theory, Oxford Univ. Press.

Bader, R. F., 2007. Everyman's derivation of the theory of atoms in molecules. J. Phys. Chem. A 111, 7966–7972.

Bindi, L., Sharp, T.G., Xie, X., 2020. Evidence for the charge disproportionation of iron in extraterrestrial bridgmanite. Sci. Adv.6, 7893.

Bolfan-Casanova, N., Keppler, H., Rubie, D. C., 2003. Water partitioning at 660 km depth and evidence for very low water solubility in magnesium silicate perovskite. Geophys. Res. Lett. 30, 172003.

Chanyshev A. , Fei, H., Bondar, D., Wang, B., Liu, Z., Ishii, T., Farla, R., McCammon, C., Katsura, T., 2023. Ferric Iron Substitution Mechanism in Bridgmanite under SiO2-Saturated Conditions at 27 GPa. ACS Earth and Space Chemistry 7 (2), 471-478

Dalou, C., Hirschmann, M. M., von der Handt, A., Mosenfelder, J., Armstrong, L. S., 2017. Nitrogen and carbon fractionation during core–mantle differentiation at shallow depth. Earth Planet. Sci. Lett. 458, 141–151.

Denbigh, K. 1981. The principles of chemical equilibrium. Cambridge University Press.

Dorfman, S. M., Nabiei, F., Boukaré, C.-E., Prakapenka, V. B., Cantoni, M., Badro, J., Gillet, P., 2021. Composition and pressure effects on partitioning of ferrous iron in iron-rich lower mantle heterogeneities. Minerals 11, 512.

Dovesi, R., Erba, A., Orlando, R., Zicovich-Wilson, C. M., Civalleri, B., Maschio, L., Rérat, M.; Casassa, S., Baima, J., Salustro, S., Kirtman, B., 2018. Quantum-mechanical condensed matter simulations with CRYSTAL. WIREs Computational Molecular Science, e1360.

Fei, H., Liu, Z., McCammon, C., Katsura, T. 2020. Oxygen vacancy substitution linked to ferric iron in bridgmanite at 27 GPa. Geophysical Research Letters, 47, e2019GL086296.

Fischer, R. A., Campbell, A. J., Reaman, D. M., Miller, N. A., Heinz, D. L., Dera, P., Prakapenka, V. B., 2013. Phase relations in the Fe–FeSi system at high pressures and temperatures. Earth Planet. Sci. Lett. 373, 54–64.

Foley, S.F., 2011. A Reappraisal of Redox Melting in the Earth's Mantle as a Function of Tectonic Setting and Time. J. Petrol. 52, 1363–1391.

Frost, D. J., Liebske, C., Langenhorst, F., McCammon, C. A., Trønnes, R. G., Rubie D. C., 2004. Experimental evidence for the existence of iron-rich metal in the Earth's lower mantle. Nature 248, 409–412.

Frost, D. J., Myhill, R., 2016. Chemistry of the Lower Mantle, in: Terasaki, H., Fischer, R.A. (eds.) Deep Earth: Physics and Chemistry of the Lower Mantle and Core. American Geophysical Union, John Wiley & Sons, Inc. Editors.

Frost, D.J., McCammon, C.A, 2008. The redox state of Earth's mantle. Annu. Rev. Earth Planet. Sci. 36, 389–420.

Fu, S., Yang, J., Karato, S.-i., Vasiliev, A., Presniakov, M. Y., Gavriliuk, A. G., Ivanova, A.G., Hauri, E. K., Okuchi, T., Purevjav, N., Lin, J.-F. (2019). Water concentration in single-crystal (Al,Fe)-bearing bridgmanite grown from the hydrous melt: Implications for dehydration melting at the topmost lower mantle. Geophysical Research Letters, 46, 10346-10357.

Fu, S., Chariton, S., Zhang, Y., Okuchi, T., Prakapenka,V.B., Lin J-F., ; Single-crystal X-ray diffraction on the structure of (Al,Fe)-bearing bridgmanite in the lower mantle. American Mineralogist 2024;109 (5): 872–881.

Grüninger, H., Liu, Z., Siegel, R., Boffa Ballaran, T., Katsura, T., Senker, J., Frost, D., 2019. Oxygen vacancy ordering in aluminous bridgmanite in the Earth's lower mantle. Geophys. Res. Lett. 46, 8731–8740.

Hazen, R.M, Downs, R.T., Jones, A.P., Kah, L., 2013. Carbon mineralogy and crystal chemistry. Rev. Mineral. Geochem. 75, 7–46.

He, Y., Duck Young K., Struzhkin, V.V, Geballe, Z.M., Prakapenka, V., Mao, H-K, 2023. The stability of FeHx and hydrogen transport at Earth's core mantle boundary. Sci. Bull. 68, 1567–1573.

Hidayat, T., Shishin, D., Jak, E., Decterov, S.A. (2015) Thermodynamic reevaluation of the Fe–O system. Calphad, 48, 131-144.

Hirschmann, M.M., 2016. Constraints on the early delivery and fractionation of Earth's major volatiles from C/H, C/N, and C/S ratios. Am. Mineral. 101, 540–553.

Hirschmann, M.M., 2018. Comparative deep Earth volatile cycles: the case for C re-cycling from exosphere/mantle fractionation of major (H_2O, C, N) volatiles and from H2O/Ce, CO2/Ba, and CO2/Nb exosphere ratios. Earth Planet. Sci. Lett. 502, 262–273.

Hou, M., He, Y., Jang, B.G., Sun, S., Zhuang, Y., Deng, L., Tang, R., Chen, J., Ke, F., Meng, Y., Prakapenka, V.B., Chen, B., Shim, J.H., Liu, J., Kim, D.Y., Hu, Q., Pickard, C.J., Needs, R.J., Mao, H.-K., 2021. Superionic iron oxide-hydroxide in Earth's deep mantle. Nat. Geosci. 14, 174–178.

Hu, Q. et al., 2016.FeO_2 and FeOOH under deep lower-mantle conditions and Earth's oxygen–hydrogen cycles. Nature 534, 241

Hu, Q., Mao, H-K., 2021. Role of hydrogen and proton transportation in Earth's deep mantle. Matter Radiat. Extremes 6, 068101.

Huang, R., Boffa Ballaran, T., McCammon, C.A., Miyajima, N., Dolejš, D., Frost D.J., 2021. The composition and redox state of bridgmanite in the lower mantle as a function of oxygen fugacity Geochimica et Cosmochimica Acta, 303,110-136.

Irifune, T., Shinmei, T., McCammon, C. A., Miyajima, N., Rubie, D. C., Frost, D. J., 2010. Iron partitioning and density changes of pyrolite in Earth's lower mantle. Science 327, 193–195.

Ismailova, L., Bykova, E., Bykov, M., Cerantola, V., McCammon, C., Boffa Ballaran, T., Bobrov, A., Sinmyo, R., Dubrovinskaia, N., Glazyrin, K., Liermann,H-P., Kupenko, I., Hanfland, M., Prescher, C., Prakapenka, V., Svitlyk,V. Dubrovinsky, L., 2016. Stability of Fe, Al-bearing bridgmanite in the lower mantle and synthesis of pure Fe-bridgmanite. Sci. Adv. 2, e1600427.

Javoy, M., Kaminski E., Guyot, F., Andrault, D., Sanloup, C., Moreira, M., Labrosse, S. , Jambon, A., Agrinier, P., Davaille, A., Jaupart, C., 2010. The chemical composition of the Earth: Enstatite chondrite models. Earth Planet. Sci. Lett. 293, 259–268.

Johnston, D.C., 2014. Advances in Thermodynamics of the van der Waals Fluid. Morgan & Claypool Publishers.

Kaminsky, F. V., Ryabchikov, I. D., McCammon, C. A., Longo, M., Abakumov, A. M., Turner, S., Heidari, H., 2015. Oxidation potential in the Earth's lower mantle as recorded by ferropericlase inclusions in diamond. Earth Planet. Sci. Lett., 417, 49–56.

Kaminsky, F.V., Lin, J-F., 2017. Iron partitioning in natural lower-mantle minerals: Toward a chemically heterogeneous lower mantle. Am. Mineral. 102, 824–832.

Karen, P., McArdle, P., Takats, J., 2016. Comprehensive definition of oxidation state (IUPAC Recommendations 2016). Pure Appl. Chem. 88, 831–839.

Katsura, T., Yoneda, A., Yamazaki, D., Yoshino, T., Ito, E., 2010. Adiabatic temperature profile in the mantle. Phys. Earth Planet. Inter. 183, 212–218.

Kröger, F. A., 1972. The Chemistry of Imperfect Crystals. North-Holland Publishing Company-Amsterdam.

Kubo, T., Kamura, K., Imamura, M. et al. 2022. Back-transformation processes in high-pressure minerals: implications for planetary collisions and diamond transportation from the deep Earth. Prog Earth Planet Sci 9, 21.

Kupenko, I., McCammon, C., Sinmyo, R., Cerantola, V., Potapkinc, V., Chumakova, A.I., Kantora, A., Rüffera, R., Dubrovinsky, L., 2015. Oxidation state of the lower mantle: In situ observations of the iron electronic configuration in bridgmanite at extreme conditions. Earth Planet. Sci. Lett. 423, 78–86. 27.

Kurnosov, A., Marquardt1, H., Frost, D. J., Boffa Ballaran, T., Ziberna, L., 2017. Evidence for a Fe^{3+}-rich pyrolitic lower mantle from (Al,Fe)-bearing bridgmanite elasticity data. Nature 543, 543–546.

Kurokawa, H., Laneuville, M., Li, Y., Zhang, N., Fujii, Y., Sakuraba, H., et al. (2022). The origin of Earth's mantle nitrogen: Primordial or early biogeochemical cycling? Geochemistry, Geophysics, Geosystems, 23, e2021GC010295.

Lavina, B. and Meng, Y 2015. Unraveling the complexity of iron oxides at high pressure and temperature: synthesis of Fe_5O_6. Sci. Adv. 1, e1400260.

Li, G., Bai, W., Shi, N., Fang, Q., Xiong, M., Yang, J., Ma, Z., Rong, H., 2012. Linzhiite, FeSi2, a redefined and revalidated new mineral species from Luobusha, Tibet, China. Eur. J. Miner. 24, 1047–1052.

Li, Y., Dasgupta, R., Tsuno, K. 2017. Carbon contents in reduced basalts at graphite saturation: implications for the degassing of Mars, Mercury, and the Moon: carbon in reduced planetary basalts. J Geophys Res Planets 122:1300–1320.

Liu, Z.D., Irifune,T., Nishi, M., Tange,Y., Arimoto, T., Shinmei, T., 2016. Phase relations in the system $MgSiO_3$– Al_2O_3 up to 52 GPa and 2000 K. Phys. Earth Planet. In., 257, 18-27

Lord, O. T., Walter, M. J., Dobson, D. P., Armstrong, L., Clark, S. M., Kleppe, A., 2010. The FeSi phase diagram to 150 GPa. J. Geophys. Res. 115, B06208.

Mao, H.-K., Hu, Q., Yang, L., Liu, J., Kim, D.Y., Meng, Y., Zhang, L., Prakapenka, V.B., 2017. Yang, W., Mao, W.L. When water meets iron at Earth's core-mantle boundary. Natl Sci Rev 4, 870–878.

Mao, H. K., Bell, P. M. 1977. Disproportionation equilibrium in iron bearing systems at pressures above 100 kbar with applications to chemistry of the Earth's mantle, in: Saxena S. K. et al. (eds.), Energetics of Geological Processes, Springer-Verlag New York Inc.

Marty, B., 2012. The origins and concentrations of water, carbon, nitrogen and noble gases on Earth. Earth Planet. Sci. Lett. 313–314, 56–66.

Mashino, I., Murakami, M., Miyajima, N., Petitgirard, S., 2020. Experimental evidence for silica-enriched Earth's lower mantle with ferrous iron dominant bridgmanite. Pr. Nat. Ac. Sc. (PNAS) 117, 27899–27905.

McCammon, C.A., Stachel, T., Harris, J.W, 2004. Iron oxidation state in lower mantle mineral assemblages: II. Inclusions in diamonds from Kankan, Guinea, 2004. Earth Planet. Sci. Lett. 222, 423–434.

McDonough, W. F., 2016. The composition of the lower mantle and core, in: Terasaki, H., Fischer, R.A. (eds.) Deep Earth: Physics and Chemistry of the Lower Mantle and Core American Geophysical Union, John Wiley & Sons, Inc. Editors.

Mergner, V., Kupenko, I., Spiekermann, G., Petitgirard, S., Libon, L., Chariton, S., Krug, M., Steinbrügge, R., Sergueev, I., Sanchez-Valle, C., 2021. Sound velocities in FeSi at lower mantle conditions and the origin of ultralow-velocity zones. Geophys. Res. Lett. 48, e2020GL092257.

Merli, M., Bonadiman, C., Diella, V., Pavese, A., 2016. Lower mantle hydrogen partitioning between periclase and perovskite: A quantum chemical modelling. Geochim. Cosmochim. Acta 173, 304–318.

Merli, M., Bonadiman, C., Diella, V., Sciascia, L., Pavese, A., 2017. Fe-periclase reactivity at Earth's lower mantle conditions: Ab-initio geochemical modelling. Geochim. Cosmochim. Acta 214, 14–29.

Merli, M., Pavese, A., 2018. Electron-density critical points analysis and catastrophe theory to forecast structure instability in periodic solids. Acta Crystallogr A Found Adv. 74, 102–111.

Merli, M., Bonadiman, C., Pavese, A., 2020. Aluminium distribution in an Earth's non–primitive lower mantle. Geochim. Cosmochim. Acta 276, 70–91.

Mohn, C.E., Trønnes, R.G., 2016. Iron spin state and site distribution in FeAlO3-bearing bridgmanite. Earth Planet. Sci. Letters 440, 178-186.

Murakami, M., Hirose, K., Kawamura, K., Sata, N., Ohishi, Y., 2004. Post-perovskite phase transition in $MgSiO_3$. Science 304, 855–858.

Oganov, A. R., Glass, C. W., 2006. Crystal structure prediction using ab initio evolutionary techniques: Principles and applications. J. Chem. Phys. 124, 244704.

Ohtani, E., Amaike, Y., Kamada, S., Sakamaki, T., Hirao. N., 2014. Stability of hydrous phase $HMgSiO_4H_2$ under lower mantle conditions. Geophys. Res. Lett.,41, 8283–8287.

Ohtani E., 2021. Hydration and dehydration in Earth's interior. Annu Rev Earth Planet Sci 49, 253–278.

Otsuka K., Longo M., McCammon M.A., Karato S., 2013. Ferric iron content of ferropericlase as a function of composition, oxygen fugacity, temperature and pressure: Implications for redox conditions during diamond formation in the lower mantle. Earth and Planetary Science Letters 365, 7-16.

Panero, W.R., Pigott, J.S., Reaman, D.M., Kabbes, J.E., Liu, Z., 2015. Dry $(Mg,Fe)SiO_3$ perovskite in the Earth's lower mantle. J. Geophys. Res. 120.

Piet, H., Badro, J., Nabiei, F., Dennenwaldt, T., Shim, S-H., Cantoni, M., Hébert, C., Gillet, P., 2016. Spin and valence dependence of iron partitioning in Earth's deep mantle. Pr. Nat. Ac. Sc. (PNAS) 113 (40), 11127-11130.

Piet, H., Chizmeshya, A., Chen, B., Chariton, S., Greenberg, E., Prakapenka, V., Buseck, P., Shim, S-H, 2023. Superstoichiometric alloying of H and close-packed Fe-Ni metal under high pressures: Implications for hydrogen storage in planetary core. Geophysical Research Letters, 50, e2022GL101155.

Prescher, C., Langenhorst, F., Dubrovinsky, L. S., Prakapenka, V. B., Miyajima, N., 2014. The effect of Fe spin crossovers on its partitioning behavior and oxidation state in a pyrolitic Earth's lower mantle system. Earth Planet. Sci. Lett. 399, 86–91.

Purevjav, N., Tomioka, N., Yamashita, S., Shinoda, K., Kobayashi, S., Shimizu, K., Ito, M., Fu, S., Gu, J., Hoffmann, C., Lin, J.-F., Okuchi, T. (2024) Hydrogen incorporation mechanism in the lower-mantle bridgmanite. American Mineralogist, 109 (6): 1036–1044.

Qian, G-R., Niu, H., Hu, C-H., Oganov, A. R., Zeng, Q., Zhou, H-Y., 2016. Diverse chemistry of stable hydronitrogens, and implications for planetary and materials sciences. Sci. Rep. 6, 25947.

Sakai, T., Ohtani, E. Terasaki, H., Sawada, N., Kobayashi, Y., Miyahara, M., 2 MasahikO Nishijima, M., Hirao, N., Ohishi, Y., Kikegawa, T. 2009. Fe-Mg partitioning between perovskite and ferropericlase in the lower mantle. American Mineralogist, 94, 921–925.

Shcheka, S. S., Wiedenbeck, M., Frost, D.J., Keppler, H. (2006) Carbon solubility in mantle minerals. Earth and Planetary Science Letters, 245, 3–4, 730-742.

Shim, S.-H., Grocholski, B., Ye, Y., Alp, E.E., Xu, S., Morgan, D., Meng, Y., Prakapenka, V.B., 2017. Stability of ferrous-iron-rich bridgmanite under reducing midmantle conditions. Pr. Nat. Ac. Sc. (PNAS) 114, 6468–6473.

Sinmyo, R., Hirose, K., 2013 Iron partitioning in pyrolitic lower mantle. Phys Chem Minerals, 40, 107–113.

Sinmyo, R., Hirose, K., Muto, S., Ohishi, Y., and Yasuhara, A., 2011. The valence state and partitioning of iron in the Earth's lowermost mantle. J. Geophys. Res., 116, B07205.

Sinmyo, R., McCammon, C., Dubrovinsky, L., 2017. The spin state of Fe^{3+} in lower mantle bridgmanite. Am. Mineral. 102, 1263–1269.

Sun, C., Dasgupta, R., 2023. Carbon budget of Earth's deep mantle constrained by petrogenesis of silica-poor ocean island basalts. Earth Planet. Sci. Lett. 611, 118135.

Tsuchiya, J., Thompson, E.C., 2022. The role of hydrogen bonds in hydrous minerals stable at lower mantle pressure conditions. Prog. Earth Planet. Sci. 9, 63.

Wang, Y., Xu, M., Yang, L. L., Yan, B., Qin, Q., Shao, Y., Zhang, Y., Huan, D., Lin, X., Lv, J., Zhang, D., Gou, H., Mao, H.-k., Changfeng, C., Ma, Y., 2020. Pressure-stabilized divalent ozonide CaO_3 and its impact on Earth’s oxygen cycles. Nat. Commun. 11, 4702.

Warr, L.N., 2021. IMA–CNMNC approved mineral symbols. Mineral. Mag. 85, 291–320.

Yang, Y.-N., Du, Z., Lu, W., Qi, Y., Zhang, Y.-Q., Zhang, W.-F. and Zhang, P.-F. (2023) NanoSIMS analysis of water content in bridgmanite at the micron scale: An experimental approach to probe water in Earth’s deep mantle. Front. Chem. 11:1166593.

Yoshioka, T., Wiedenbeck M., Shchek, S., Keppler, H., 2018. Nitrogen solubility in the deep mantle and the origin of Earth’s primordial nitrogen budget. Earth Planet. Sci. Lett. 488, 134–143.

Zakeri, A., Coley, K.S., Tafaghodi, L. (2023) Hydrogen-Based Direct Reduction of Iron Oxides: A Review on the Influence of Impurities. Sustainability, 15, 13047.

Zhang, F., Oganov, A. R., 2006. Valence state and spin transitions of iron in Earth's mantle silicates. Earth Planet. Sci. Lett. 249, 436–443.

Zhang, L., Chen, Y., Yang, Z., Liu, L., Yang, Y., Dalladay-Simpson, P., Wang, J., Mao, H. (2024) Pressure stabilizes ferrous iron in bridgmanite under hydrous deep lower mantle conditions. Nat Commun 15, 4333.

Figure 1

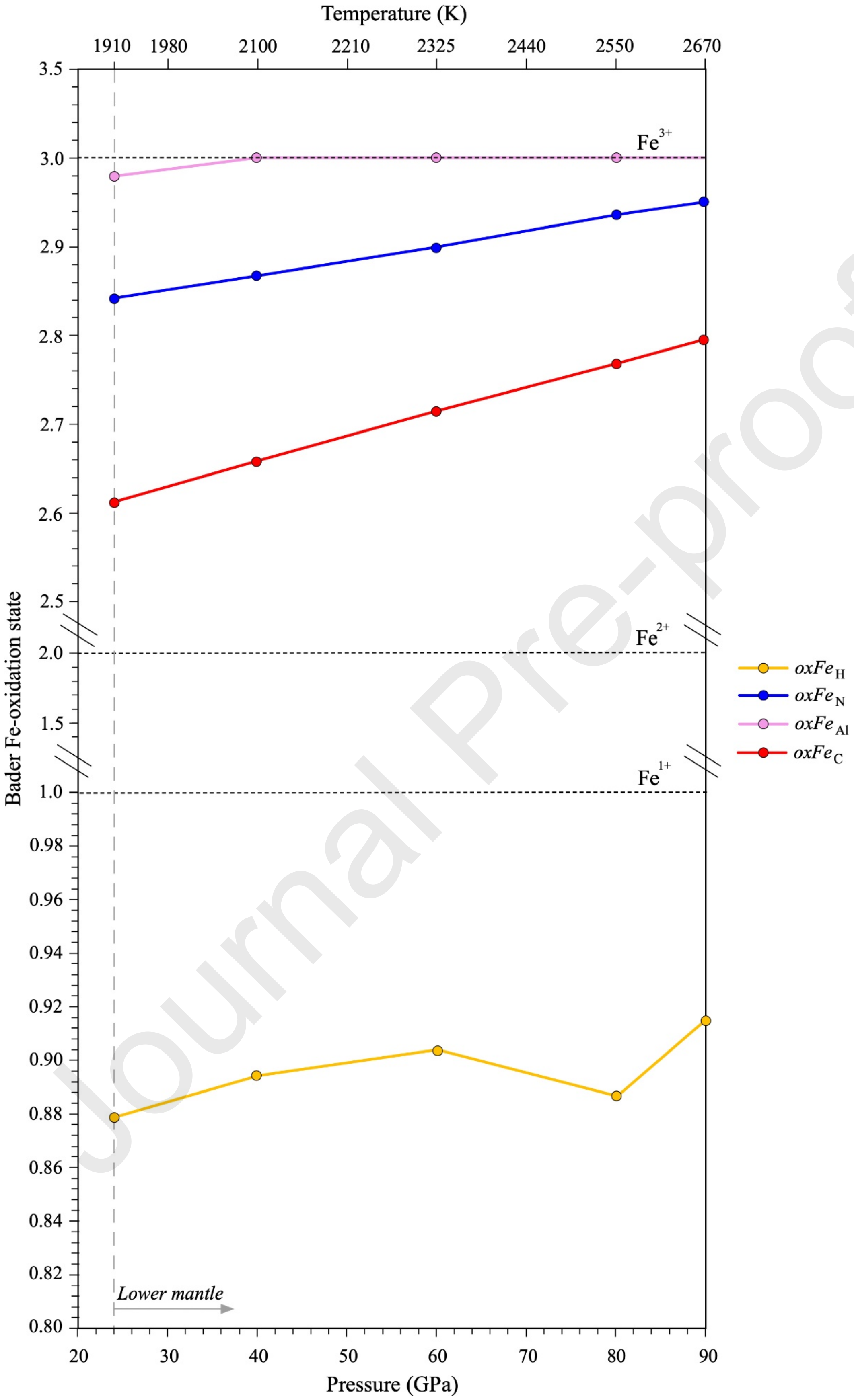
Temperature (K)
1910
1980
2100
2210
2325
2440
2550
2670
3.5
3.0
2.9
2.8
2.7
2.6
2.5
2.0
1.5
1.0
0.98
0.96
0.94
0.92
0.90
0.88
0.86
0.84
0.82
0.80
Fe^{3+}
Fe^{2+}
Fe^{1+}
Bader Fe-oxidation state
Lower mantle
20
30
40
50
60
70
80
90
Pressure (GPa)
$oxFe_H$
$oxFe_N$
$oxFe_{Al}$
$oxFe_C$

Figure 1. Bader oxidation state of Fe in bridgmanite (Bdm) as function of *P*. *oxFe*, calculated using the atomic basin charges and equ.(4.b), as a function of each species incorporated (H, N, Al and C). The atomic basin of a given atom is the region around it confined by the related Ω-surface, the latter defined in section 2.1 "Oxidation state modelling". The reported *T* values correspond to the geotherms of Katsura et al. (2010) and Merli et al. (2016). Symbols: values by calculations.

Figure 2

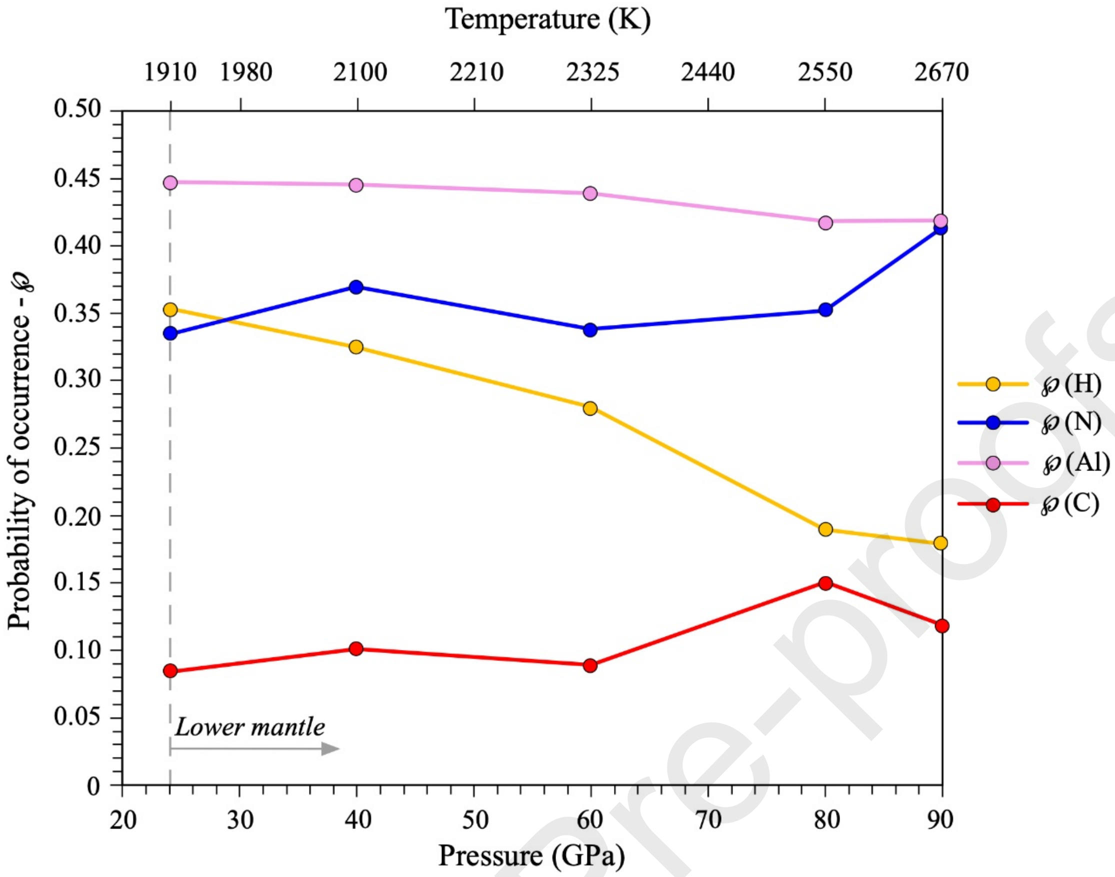
Temperature (K)
1910
1980
2100
2210
2325
2440
2550
2670
Probability of occurrence - ℘
0.50
0.45
0.40
0.35
0.30
0.25
0.20
0.15
0.10
0.05
0
Lower mantle
20
30
40
50
60
70
80
90
Pressure (GPa)
℘ (H)
℘ (N)
℘ (Al)
℘ (C)

Figure 2. Probability of incorporation in Bdm of H, N, Al and C, $\wp$ (H, N, Al, C), as function of *P*-*T* determined according to the redox reactions (3.a-d). $\wp$ (H, N, Al, C) estimates the tendency of each reaction to develop rightwards, *i.e.*, towards incorporation, *via* the equilibrium constant, *K*, and equ.B.4 in Supplementary Material B. In this view, $\wp$ (H, N, Al, C) can be likened to a measure of the occurrence of the H/N/Al/C-uptake in Bdm. Symbols: values by calculations.

Figure 3

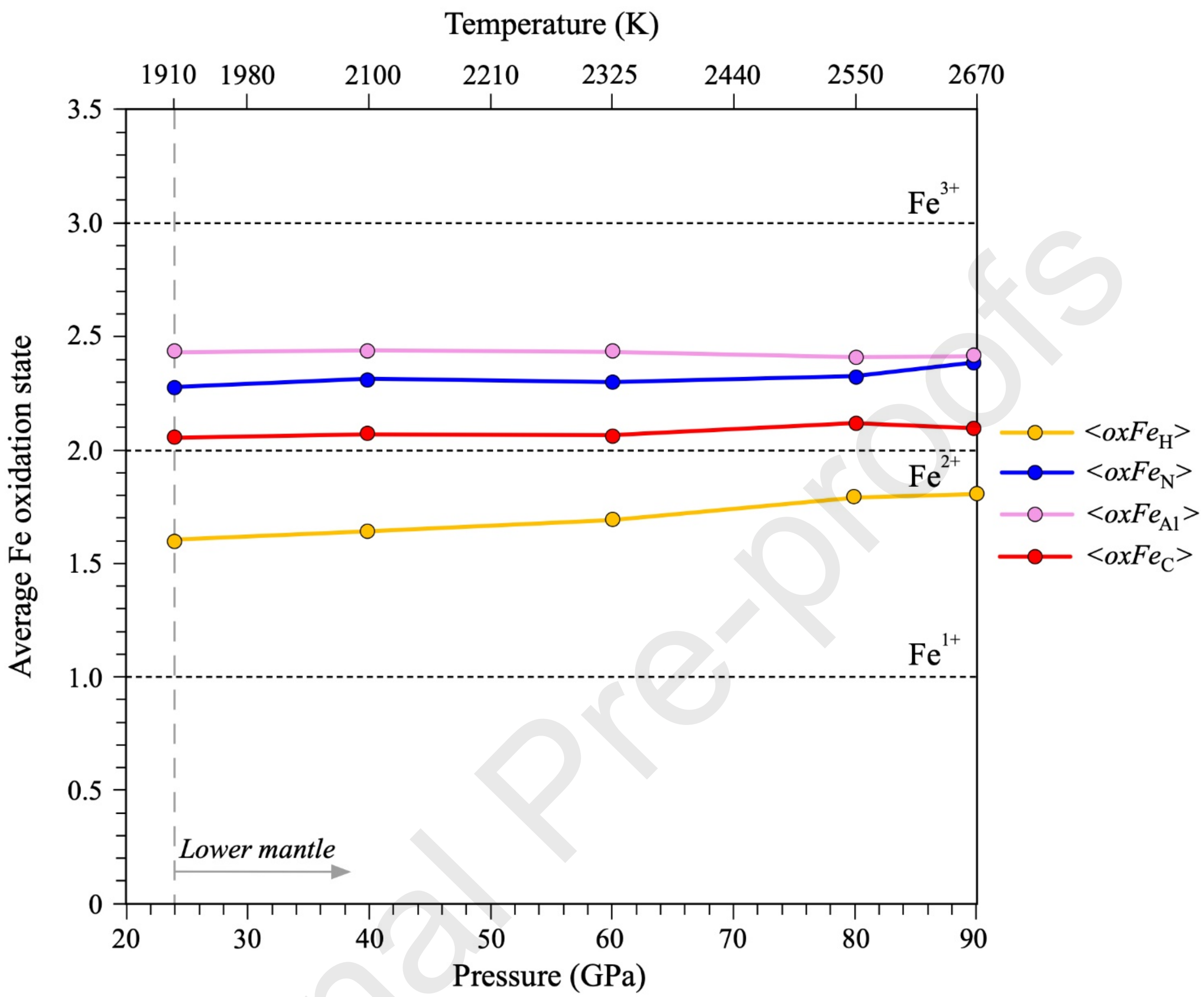
Temperature (K)
1910
1980
2100
2210
2325
2440
2550
2670
3.5
3.0
2.5
2.0
1.5
1.0
0.5
0
Average Fe oxidation state
Fe^{3+}
Fe^{2+}
Fe^{1+}
Lower mantle
20
30
40
50
60
70
80
90
Pressure (GPa)
<$oxFe_H$>
<$oxFe_N$>
<$oxFe_{Al}$>
<$oxFe_C$>

Figure 3. Average iron oxidation state corresponding to the actual Fe oxidation state in Bdm, <$oxFe_{\mathrm{H,N,Al,C}}$>, calculated using equ.(5.a), as a function of each species incorporated (H, N, Al and C) and of *P*-*T*. <$oxFe_{\mathrm{H,N,Al,C}}$> depends on the Bader oxidation state (Fig. 1) and on the probability that the related oxidizing reaction occurs (Fig. 2). In this light, the average Fe oxidation state provides an estimate of the actual oxidation number of iron. Symbols: values by calculations.

Figure 4

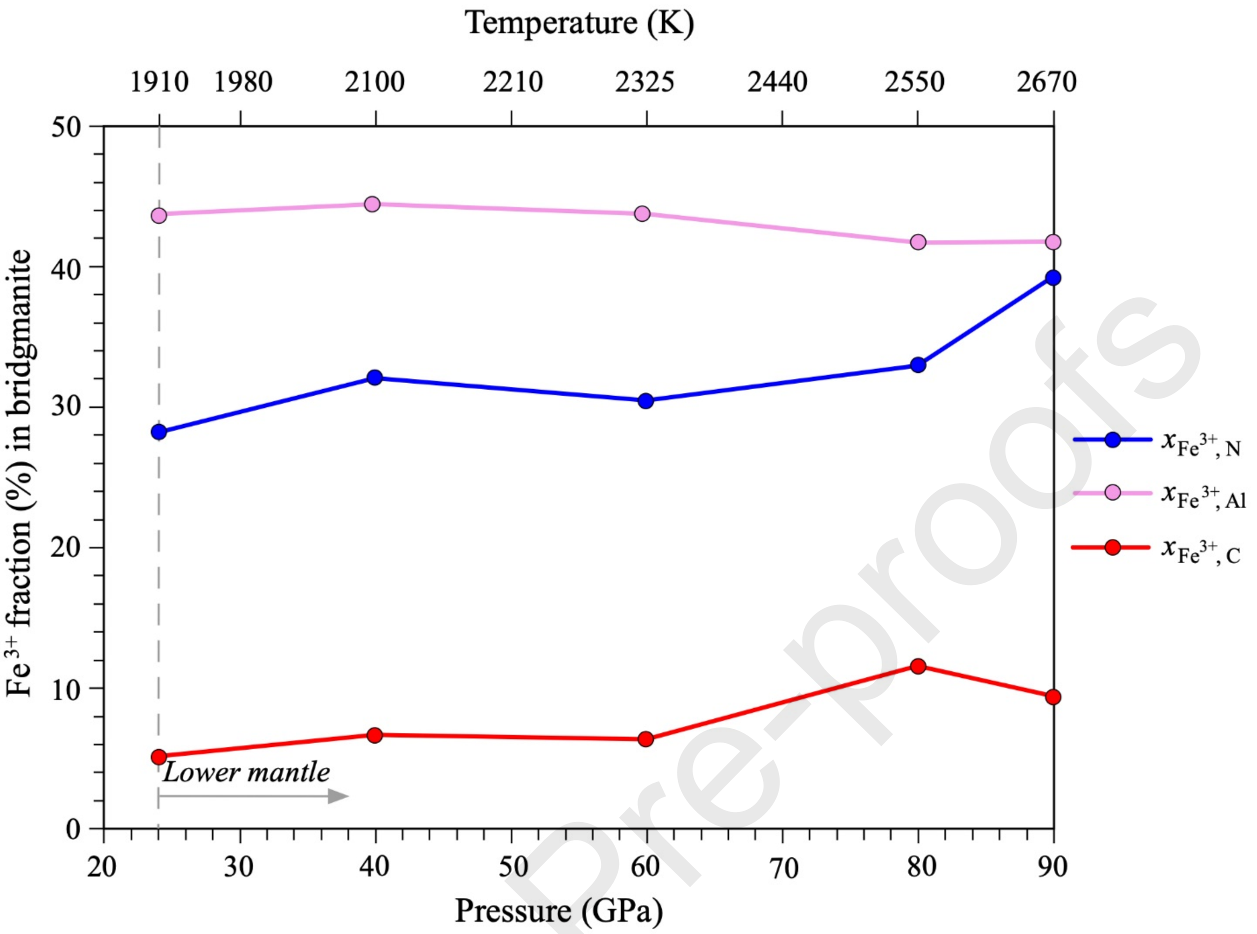
Temperature (K)
1910
1980
2100
2210
2325
2440
2550
2670
50
40
30
20
10
0
Fe^{3+} fraction (%) in bridgmanite
Lower mantle
20
30
40
50
60
70
80
90
Pressure (GPa)
$x_{\mathrm{Fe}^{3+},\mathrm{N}}$
$x_{\mathrm{Fe}^{3+},\mathrm{Al}}$
$x_{\mathrm{Fe}^{3+},\mathrm{C}}$

Figure 4. Fe^{3+} fractions in bridgmanite (Fe^{3+}/Fe_{Bdm}) ascribable to Al, N and C, *i.e*., reactions (3.b,c,d), as function of *P*-*T*, and calculated through the average iron oxidation state provided by $<oxFe_{N,Al,C}>$, using equ.(7). The Fe^{3+}/Fe_{Bdm} figures are independent of the availability of the involved species in the lower mantle system. In this view, the ferric fractions so determined reflect the maximum oxidizing action of each of the species incorporated (Al, N and C). Hydrogen is not shown as it induces reduction of iron (see Fig. 3), and therefore it gives a negative contribution in terms of x_{Fe3+}. Symbols: values by calculations.

Figure 5

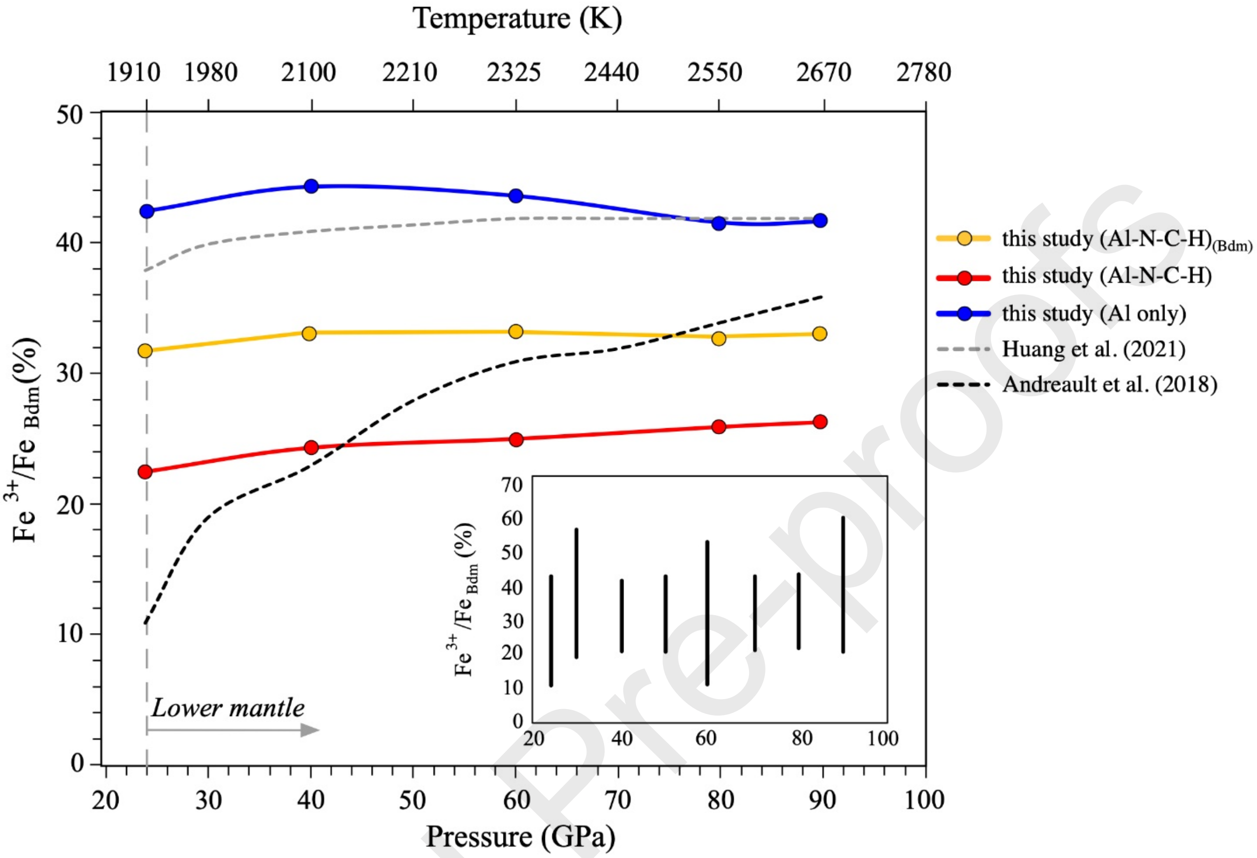
Temperature (K)
1910
1980
2100
2210
2325
2440
2550
2670
2780
Fe 3+/Fe Bdm(%)
0
10
20
30
40
50
Lower mantle
20
30
40
50
60
70
80
90
100
Pressure (GPa)
Fe 3+/Fe Bdm (%)
0
10
20
30
40
50
60
70
20
40
60
80
100
this study (Al-N-C-H)(Bdm)
this study (Al-N-C-H)
this study (Al only)
Huang et al. (2021)
Andreault et al. (2018)

Figure 5. The fraction (%) of ferric iron in Bdm (Fe^{3+}/Fe_{Bdm}) [equ.(6-7)], as a function of *P-T*. Fe^{3+}/Fe_{Bdm} with the contributions of Al-N-C-H (red line; H-content as large as 221 ppm) and (yellow line; H-content as large as 112 ppm) are compared with that modelled neglecting the N-C-H effects (blue line). The Fe^{3+}/Fe_{Bdm} ratios are compared with those experimentally obtained for Al-bearing Bdm of similar composition in the same *P* range of this study by Huang et al. (2021); grey dotted line) and Andreault et al. (2018); black dashed line. A set of Fe^{3+}/Fe_{Bdm} early determinations is displayed as a function of pressure in the range explored in this study, to show the scattering of data (inset). A comparison of our results with the extant Fe^{3+}/Fe_{Bdm} experimental values is difficult because of the complexity of several aspects, such as experimental setup, starting material and Bdm compositions. Al-bearing bridgmanite data set is from Shim et al. (2017), Piet et al. (2016) Kupenko et al. (2015), Prescher et al. (2014), Sinmyo et al. (2011), Andrault et al. (2018), Huang et al. (2021) Chanyshev et al. (2023); Zhang et al. (2024). Symbols: values by calculations.

Figure 6

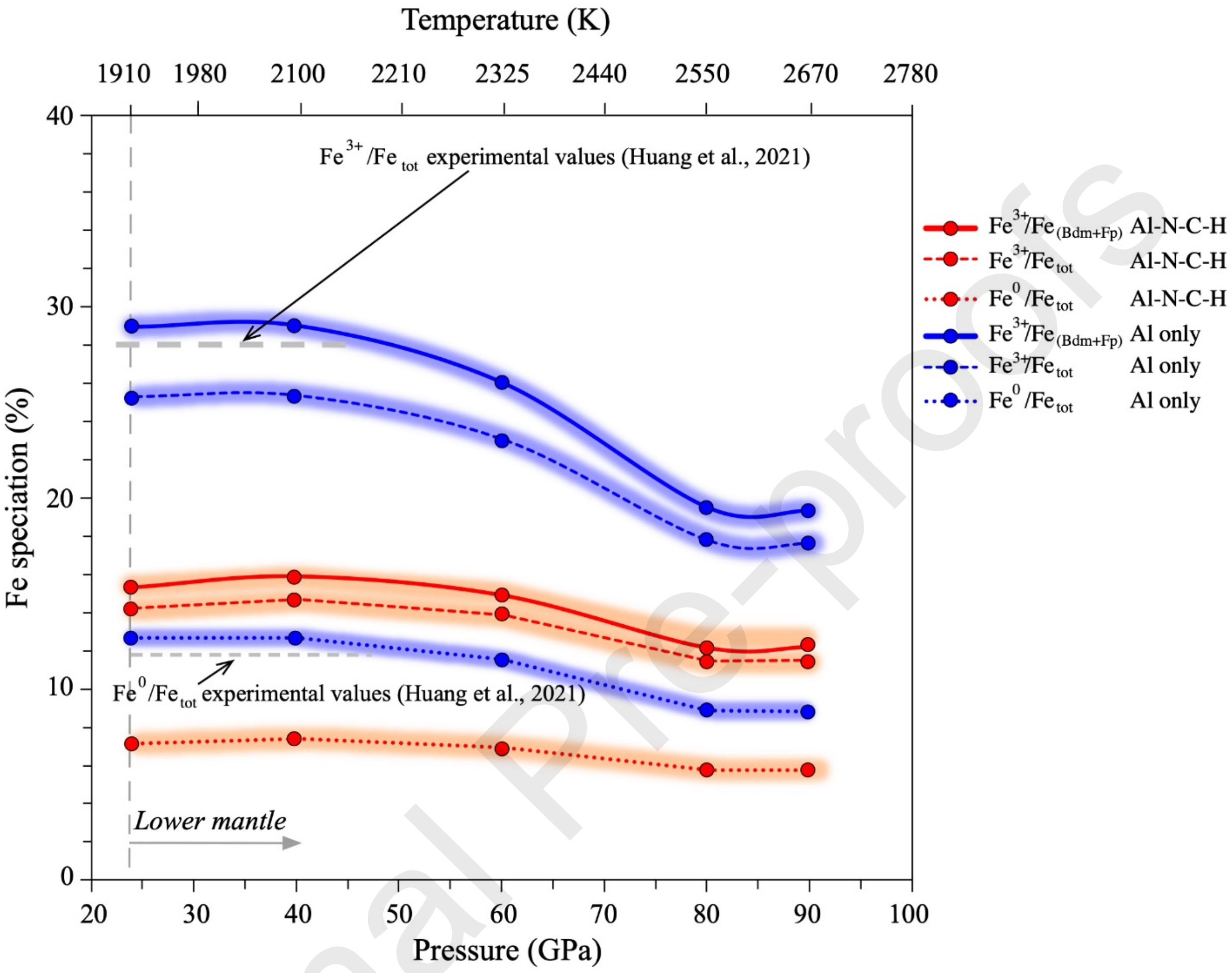
Temperature (K)
1910
1980
2100
2210
2325
2440
2550
2670
2780
Fe speciation (%)
0
10
20
30
40
Pressure (GPa)
20
30
40
50
60
70
80
90
100
Fe^{3+}/Fe_{tot} experimental values (Huang et al., 2021)
Fe^{0}/Fe_{tot} experimental values (Huang et al., 2021)
Lower mantle
$Fe^{3+}/Fe_{(Bdm+Fp)}$ Al-N-C-H
Fe^{3+}/Fe_{tot} Al-N-C-H
Fe^{0}/Fe_{tot} Al-N-C-H
$Fe^{3+}/Fe_{(Bdm+Fp)}$ Al only
Fe^{3+}/Fe_{tot} Al only
Fe^{0}/Fe_{tot} Al only

Figure 6. $Fe^{3+}/Fe_{(Bdm+Fp)}$, Fe^{3+}/Fe_{tot} and Fe^0/Fe_{tot} (Fe_{tot}=Fe^{2+}+Fe^{3+}+Fe^0) in bulk lower mantle as a function of *P*-*T* modelled with the redox contribution of Al-N-C-H (red patterns; H-content as large as 221 ppm) and Al-only (blue patterns). $Fe^{3+}/Fe_{(Bdm+Fp)}$ is calculated by <*oxFe*> of equ.(6), for the total average oxidation state of iron, and equ.(7), for the partitioning between Fe^{2+} and Fe^{3+}. Iron is partitioned between Bdm and Fp using the *K*d calculated by Merli et al. (2017). Hydrogen is distributed over Bdm and Fp using the coefficient provided by Merli et al. (2016). Fe^0 is calculated assuming its formation entirely due to disproportionation reaction ($3Fe^{2+}\rightarrow 2Fe^{3+}+Fe^0$). Fe_{tot} = 6.3 wt% (Supplementary material D). The shadow field of each line represents the degree of confidence of the model (~8%). The experimentally obtained Fe^{3+}/Fe_{tot} and Fe^0/Fe_{to} values using lower mantle bulk iron = 6.1 wt% and Al-in-Bdm contents of 0.07 (*P* = 24-50 GPa) are reported for comparison (Huang et al., 2021). Symbols: values by calculations.

Declaration of interests

☒ The authors declare that they have no known competing financial interests or personal relationships that could have appeared to influence the work reported in this paper.

☐The authors declare the following financial interests/personal relationships which may be considered as potential competing interests: